arXiv:2508.14482v3 [cs.LG] 7 May 2026

On the notion of missingness for path attribution explainability methods in medical settings: Guiding the selection of medically meaningful baselines

Alexander Geiger[1] **Lars Wagner**[1] **Daniel Rueckert**[2,3] **Dirk Wilhelm**[1,4] **Alissa Jell**[1,4]

[1]Research Group MITI, Technical University of Munich, Germany
[2]Chair for AI in Healthcare and Medicine,
Technical University of Munich (TUM) and TUM University Hospital, Germany
[3]Department of Computing, Imperial College London, UK
[4]Department of Surgery, Technical University of Munich, Germany

Abstract

The explainability of deep learning models remains a significant challenge, particularly in the medical domain where interpretable outputs are essential for clinical trust and transparency. Path attribution methods such as Integrated Gradients rely on a baseline that represents the absence of informative features, a notion commonly referred to as *missingness*. Standard baselines, such as all-zero inputs, are often semantically meaningless in medical contexts, where intensity values carry clinical significance. In this work, we revisit the notion of missingness for medical imaging, expose the limitations of standard baselines in this setting, and formalize a stricter missingness we term *semantic missingness*: a baseline must not merely lack signal, but must represent a clinically plausible state in which the disease-related features are absent. This formulation motivates a counterfactual-guided approach to baseline selection, in which a synthetically generated counterfactual (i.e. a clinically normal variant of the pathological input) serves as a principled and semantically meaningful reference. We derive theoretical guarantees showing that counterfactual baselines yield more faithful attributions than standard alternatives, and empirically validate this with two complementary counterfactual generative models, a Variational Autoencoder and a diffusion model, though the concept is model-agnostic and compatible with any suitable counterfactual method. Across three diverse medical datasets, counterfactual baselines produce more faithful and medically relevant attributions, outperforming standard baseline choices as well as related methods. Notably, we also compare against using the counterfactual directly as an explanation (an established paradigm in its own) and show that employing it as a baseline for Integrated Gradients yields superior results, thereby bridging two complementary explainability paradigms.

1 Introduction

The integration of Artificial Intelligence (AI) into medical practice is rapidly transforming the landscape of healthcare, offering powerful tools for diagnostics, prognosis, and treatment planning. However, despite their accuracy, these models often operate as "black boxes", offering little insight into how specific predictions are made. To this end, the ability to interpret and understand the internal decision-making processes of AI models is of great importance in the medical domain and many different approaches have been developed over the years [23, 7, 43]. Among the most widely used explainability methods is Integrated Gradients (IG) [44], a path attribution technique that satisfies several desirable axioms [44, 32]. A critical component of IG, as well as other explainability concepts

Preprint.

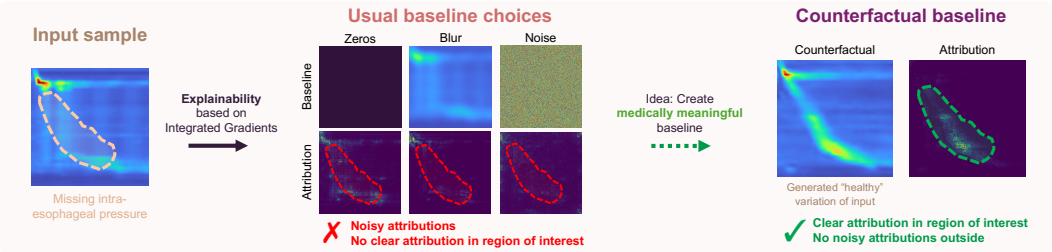


Figure 1: Effect of baseline choice on attribution quality for an pathological manometry input. Standard baselines (zeros, blurred input, random noise) yield spurious attributions outside the true region of interest, while our generated counterfactual baseline produces cleaner and more accurately localized attributions.

like DeepLift [40] and GradientSHAP [31], is the choice of a baseline reference, which ideally represents an absence ("missingness") of any relevant features. This concept of missingness is central to interpretability research [42]. A common baseline is a zero-valued input, which corresponds to a black image in computer vision tasks. However, since IG is defined to attribute differences in model output between the baseline and the input without regard to the semantic appropriateness of the baseline, such choices can lead to misleading attributions (e.g., IG is 'blind' to the baseline color). Thus, alternative baselines such as blurred inputs or random noise have been proposed [17]. Yet, these alternatives often lie outside the data distribution the model was trained on, potentially resulting in erroneous attributions due to unreliable gradients in regions of input space the model has never encountered. Therefore, Erion et al. [16] introduced Expected Gradients (EG), an extension of IG that samples multiple baselines from the training distribution and averages the resulting attributions.

Despite this advancement, we show in this work that even these data-aware baselines produce poor attributions in certain medical contexts. For example, when the class-defining feature is itself a form of missingness, standard baselines fail to capture the intended contrast. This can be observed, for instance, in esophageal manometry recordings, where pathology can be characterized by the absence of normal pressure patterns, or in chest X-rays of pneumothorax patients, where the condition can manifest as a missing lung boundary or contrast. These shortcomings indicate that a stricter notion of missingness for the baseline is required: one that does not merely encode an arbitrary or signal-free input, but also represents a clinically plausible state in which the disease-related features are genuinely absent. This motivates the central idea of our work, replacing conventional baselines with synthetically generated *counterfactual baselines* that reflect a clinically normal variant of the pathological input, thereby providing a principled and semantically meaningful reference for attribution. Fig. 1 illustrates how this aligned notion of missingness yields cleaner and more clinically relevant attributions than conventional baselines.

To our knowledge, this is the first work to systematically examine missingness in the medical context and its implications for baseline selection. We summarize our contributions as follows:

- *Formalization of semantic missingness.* We revisit the notion of missingness in the context of medical imaging, expose the limitations of standard baselines, and introduce *semantic missingness* as a stricter requirement: a baseline must not merely lack signal, but represent a clinically plausible state in which disease-related features are absent, thus motivating counterfactual baselines.
- *Theoretical analysis.* We derive formal guarantees showing why counterfactual baselines yield more faithful attributions, providing a principled justification for our concept.
- *Empirical evaluation across three medical datasets.* We compare a broad range of baselines and related concepts against our counterfactual baselines on three diverse medical imaging datasets, and demonstrate consistent improvements in both faithfulness and clinical relevance.
- *Bridging counterfactual explanations and path attribution.* We show that using a generated counterfactual as the baseline for Integrated Gradients outperforms using the counterfactual directly as the explanation itself (an established paradigm in its own), thereby connecting two previously distinct branches of the explainability literature.

Related literature Explainability methods have gained significant attention in recent years, particularly as AI systems are increasingly deployed in high-stakes domains. Broad overviews of explainable artificial intelligence (XAI) are provided by Minh et al. [34] and Angelov et al. [3], who review

general techniques and motivations for interpretability across domains. In medical settings, the need for transparency and clinical trust makes interpretability especially critical [7], and several surveys discuss both the domain-specific challenges and the adaptation of general techniques [43, 23, 46, 10].

Generative models have recently emerged as powerful tools for improving the interpretability of medical AI models, for example by translating images between domains [6] or by encoding input features into structured latent representations [5] that can be traversed to observe and explain corresponding model outputs [11, 13]. Closely related is the use of counterfactual explanations, which provide generated contrastive inputs that lead to different model outcomes and thereby offer an intuitive way to visualize the factors influencing a model's decision [39, 33, 38, 4, 45, 36, 47, 35, 19]. While counterfactuals provide such intuitive explanations on their own, we show in this work that they can be leveraged even more effectively when used as baselines for path attribution methods such as IG, which remain a cornerstone of explainability for understanding feature-level contributions.

A complementary line of research addresses noisy IG attributions by adapting the integration path. Kapishnikov et al. [25] introduce Guided Integrated Gradients, which optimizes the path along the model's output surface, while Zhuo and Ge [51] extend this by jointly deriving the path and baseline from a counter-class reference. Further geometric approaches have also been explored in this regard [49]. While these methods improve upon the linear path of standard IG, they treat the baseline as fixed and inherited, leaving semantically meaningful baseline selection unaddressed. Here, a separate line of work examines the choice of baseline itself. Dravid et al. [14] propose Latent Integrated Gradients (LIG), which uses a GAN-generated counterfactual as the baseline and computes IG in the generator's latent space. However, as LIG operates entirely in the generated domain, the actual input is never directly explained, limiting clinical interpretability. Most closely related to our work, yet in the tabular data domain, Duell et al. [15] combine IG with counterfactual baselines for tabular medical records. However, they treat the counterfactual as a given explanation rather than as a principled baseline choice, provide no comparison to alternative baselines, and no formal attribution quality assessment, thus leaving entirely open whether and why counterfactuals constitute a better baseline than standard alternatives.

Our work addresses these gaps in several ways. We provide a formal framework for why counterfactual baselines are particularly suited to medical settings, systematically compare against a broad range of alternative baselines and related approaches across three medical datasets, as well against using counterfactuals alone as explanations. Crucially, we build directly on the standard IG formulation rather than introducing adaptive paths or modified attribution computations, thereby staying faithful to the original IG definition and automatically inheriting all of its several attribution axioms.

2 Motivation

IG is an attribution method that assigns importance to each input feature by integrating the gradients of the model's output with respect to the inputs along a path from a baseline input (ideally representing an absence of any features of the target class) to the actual input. The IG for input $x \in \mathbb{R}^n$ and baseline $\hat{x} \in \mathbb{R}^n$ is defined as: $\mathrm{IG}_i(x, \hat{x}) = (x_i - \hat{x}_i) \cdot \int_{\alpha=0}^{1} \frac{\partial \mathcal{C}(\hat{x}+\alpha\cdot(x-\hat{x}))}{\partial x_i}\, d\alpha$, where $\mathcal{C} : \mathbb{R}^n \to \mathbb{R}$ is the classifier function (e.g., the output logit or probability for a specific class) and α is a scalar interpolating from $\hat{x}$ to x.

Missingness and Baseline Semantics IG explains a prediction relative to a baseline $\hat{x}$ via $\sum_{i=1}^{n} \mathrm{IG}_i(x; b) = \mathcal{C}_y(x) - \mathcal{C}_y(b)$, where the baseline represents the state in which the target concept y is "absent", defining basic missingness.

> **Definition 2.1** (Basic missingness)**.** A baseline $\hat{x}$ satisfies *basic missingness* for class y if $\mathcal{C}_y(\hat{x}) \approx 0$, i.e. the output logit is near neutral for class y.

In this sense, basic missingness just means that the baseline does not contain discriminative information for class y under the model. Standard baselines are designed with this notion in mind: zero, blurred, and noise inputs all aim to produce low classifier confidence for any specific class, and EG approximates the same goal by averaging over training-data baselines. In medical imaging, however, low classifier evidence alone does not guarantee a meaningful absence of the concept. We accordingly introduce a stricter notion that demands not only the lack of class evidence, but also semantic plausibility and structural relation to the input.

Definition 2.2 (Semantic missingness)**.** A baseline $\hat{x}$ satisfies *semantic missingness* for class y if (1) $\mathcal{C}_y(\hat{x}) \approx 0$, (2) $\hat{x} \in \mathcal{M}$, and (3) $\|\hat{x} - x\|_2$ is small.

Intuitively, a baseline $\hat{x}$ that satisfies semantic missingness represents a semantically plausible input that closely resembles x but no longer contains evidence for class y, i.e. a counterfactual.

Baseline choice in medical imaging: limitations and the case for counterfactuals With this definition in mind, several distinct shortcomings of standard baselines and corresponding advantages of counterfactual baselines emerge.

Semantically meaningful vs. merely null reference. Standard baselines aim only for low classifier evidence (condition 1), but the resulting input is typically not a semantically valid state: a zero or noise image is not something the model has ever encountered as a plausible medical input. Counterfactual baselines, by construction, represent a clinically normal variant of x and therefore provide a reference state that is meaningful in the diagnostic sense, not merely null with respect to the classifier.

On- vs. off-manifold reference and interpolation paths. Black, blurred, and noisy baselines lie far from the data manifold (violating condition 2), and EG's training-data baselines, although individually on-manifold, are anatomically unrelated to the input and therefore induce paths that pass through implausible intermediate states. Such paths are particularly problematic when pathology manifests as a subtle perturbation of normal tissue, and the effect of out-of-distribution intermediate inputs on attribution quality is poorly understood [42, 22, 17]. A counterfactual x_{normal} satisfies the manifold condition by construction and, because it is conditioned on x (condition 3), induces an interpolation path $\gamma(\alpha) = x_{\text{normal}} + \alpha(x - x_{\text{normal}})$ that transitions smoothly from a clinically normal to a pathological state, more likely to remain on the manifold.

Accidental matching of pathological values. Standard baselines are agnostic to how pathology manifests in a given input and may coincidentally match pathological intensity values. For instance, low intensities encode absent peristalsis in manometry. The result is not merely a lack of neutrality but active suppression of attribution signal in the regions of interest, since the contrast term $(x_i - \hat{x}_i)$ vanishes precisely where it should be largest. Counterfactual baselines are explicitly constructed to differ from the input in pathological regions, eliminating this failure mode and concentrating gradient signal where it is diagnostically meaningful.

3 Counterfactual baselines

We first formalize the notion of a perfect counterfactual baseline in the context of path-based attribution methods and show that, under this idealization, Integrated Gradients assigns non-zero attribution only to pathological coordinates, i.e. achieves a perfect attribution map with no spurious attributions. Let $\mathcal{C} : \mathbb{R}^n \to \mathbb{R}$ be a differentiable function representing the scalar prediction of interest (e.g., the logit for a disease class). Let $x \in \mathbb{R}^n$ be a fixed input and let $S \subseteq \{1, \ldots, n\}$ denote the (unknown) set of *pathological coordinates*, i.e., the coordinates where the input differs from a corresponding healthy, pathology-free version.

Definition 3.1 (Perfect Counterfactual Baseline)**.** A baseline $\text{CF}^* \in \mathbb{R}^n$ is called a *perfect counterfactual baseline* if $\mathcal{C}(\text{CF}^*)$ corresponds to a neutral prediction, there exists a minimal causal index set $S \subseteq \{1, \ldots, n\}$ such that $x_i = \text{CF}^*_i$ for all $i \notin S$;, and the prediction difference $\mathcal{C}(x) - \mathcal{C}(\text{CF}^*)$ depends only on coordinates in S.

Intuitively, CF^* differs from x only in those features causally responsible for the prediction. In this case, we can show that all attribution mass is concentrated on the causal coordinates S only.

Proposition 1 (Perfect Attribution under Perfect Counterfactual Baseline)**.** Let $\mathcal{C}$ be continuously differentiable and let CF^* be a perfect counterfactual baseline for x. Then (1) $\text{IG}_i(x; \text{CF}^*) = 0$ for all $i \notin S$ and (2) $\sum_{i \in S} \text{IG}_i(x; \text{CF}^*) = \mathcal{C}(x) - \mathcal{C}(\text{CF}^*)$.

This follows directly from the definitions of IG and the Perfect Counterfactual Baseline (see appendix A.1). However, in practice, a perfect counterfactual may not be available or infeasible to compute. We therefore also consider the more realistic case of approximate counterfactual baselines.

Approximate counterfactuals We show that, under mild assumptions, if an approximate counterfactual baseline $\tilde{x}$ is closer to the perfect counterfactual CF^* than another (standard) baseline b is, then the corresponding attribution $\text{IG}(x;\tilde{x})$ is closer to the ideal attribution $\text{IG}(x;\text{CF}^*)$ in terms of error upper bound than $\text{IG}(x;b)$ is.

Proposition 2 (Closeness to True Counterfactual Implies Lower Attribution Error Upper Bound)**.** Let $b \in \mathbb{R}^d$ be an arbitrary baseline. Define $\delta_b := \|b - \text{CF}^*\|_2$ and $C := \frac{L}{2}\|x - \text{CF}^*\|_2 + G_\infty$. Under assumptions (A1) and (A2) (see appendix A.2), for any baseline b,

$$\|\text{IG}(x;b) - \text{IG}(x;\text{CF}^*)\|_2 \leq C\,\delta_b.$$

Consequently, for two baselines b_1, b_2, if $\|b_1 - \text{CF}^*\|_2 < \|b_2 - \text{CF}^*\|_2$, then their corresponding worst-case upper bounds satisfy $C\|b_1 - \text{CF}^*\|_2 < C\|b_2 - \text{CF}^*\|_2$. Hence, a baseline closer to the true counterfactual admits a strictly tighter theoretical upper bound on the attribution deviation.

Proposition 2 formalizes the intuition that Integrated Gradients is stable under small perturbations of the baseline (see appendix A.2 for the full derivation). In particular, if we regard the perfect counterfactual baseline CF^* as defining an ideal, pathology-only attribution (Proposition 1), then any approximate counterfactual baseline $\hat{\text{CF}}$ that is close to CF^* in input space will, by design, yield attributions that are close to this ideal. Conversely, standard baselines b that are far from CF^*, and typically differ from x in large healthy regions, have a larger upper bound, which allows attributions to potentially deviate substantially from the ideal attribution, often exhibiting spurious importance outside the pathological region.

Additionally, in order to demonstrate this theoretical result empirically, we constructed a synthetic dataset in which the true counterfactual CF^* is known by design, enabling direct measurement of attribution quality as a function of baseline distance. As shown in Fig. 2, attribution quality degrades gradually as the baseline moves from CF^* through our generated approximations $\text{CF}_{\text{Dif.}}$ and CF_{VAE} toward the zeros baseline, substantiating the theoretical proximity-attribution relationship. We refer to Appendix B for full experimental details.

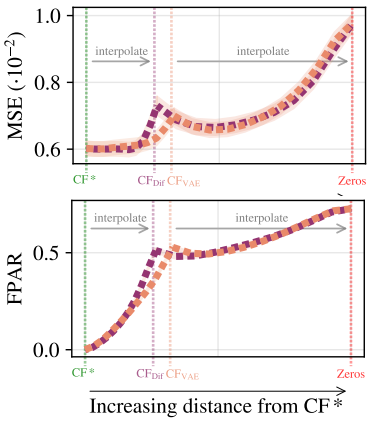


Figure 2: MSE and FPAR when increasing the distance to the perfect counterfactual CF^* by interpolating to the approximated counterfactual baselines and then to the zeros baseline.

3.1 Method: Generation of Counterfactual Baseline

We propose using generated counterfactual images as baselines for path attribution methods. While we instantiate this concept with two complementary generative approaches (a VAE-based and a diffusion-based method), the framework is model-agnostic: any counterfactual generation technique that produces anatomically plausible, disease-free variants of a pathological input can be substituted, with the potential for further gains using more advanced methods. We demonstrate our concept using two generative approaches that differ in their inductive biases and guidance mechanisms, providing evidence that the benefits of counterfactual baselines are not tied to a specific generation paradigm.

The **VAE-based approach** encodes the input x into a latent representation and optimizes the latent code toward the healthy class using classifier feedback, before decoding to obtain the counterfactual $\hat{\text{CF}}$. This constitutes a classifier-guided generation strategy operating in a compressed latent space.

The **diffusion-based approach** instead adds noise to the input up to a fixed timestep and then denoises it using a classifier-free guided diffusion model conditioned on the healthy class, steering the reconstruction away from pathological features without requiring an explicit latent optimization loop. Full implementation details for both approaches are provided in Appendix H. Together, they cover both classifier-guided and classifier-free generation strategies, further supporting the method-agnostic nature of our framework and ruling out potential circularity issues. Additionally, while our framework does not require generated counterfactuals to be perfect (Proposition 2), we nevertheless assess their quality to rule out unintended adversarial or off-manifold artifacts. Here we observe that generated

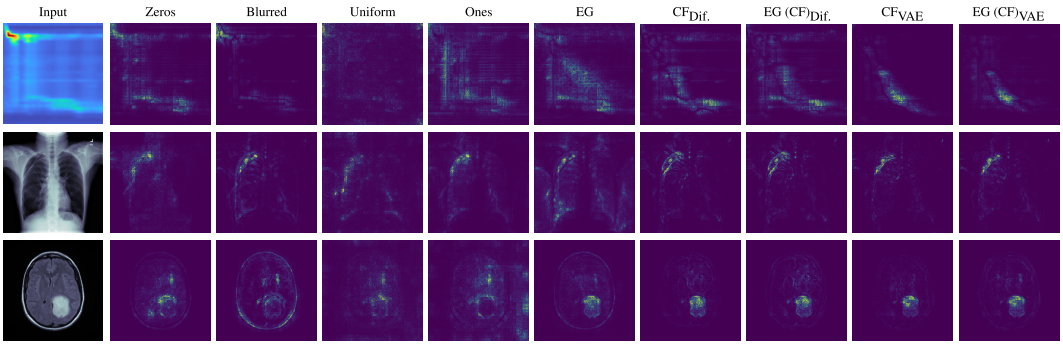


Figure 3: Examples of attributions obtained using different baselines.

counterfactuals substantially shift inputs toward the real healthy distribution while concentrating modifications in clinically relevant regions, with quantitative realism metrics reported in Appendix G.

3.2 Attribution with Counterfactual Baselines

Given a generated counterfactual $\hat{\text{CF}}$ for input x, the attribution is computed by using $\hat{\text{CF}}$ as the baseline in the standard IG formulation:

$$\text{IG}(\text{CF})_i(x) = (x_i - \hat{\text{CF}}_i) \cdot \int_{\alpha=0}^{1} \frac{\partial \mathcal{C}\left(\hat{\text{CF}} + \alpha \cdot (x - \hat{\text{CF}})\right)}{\partial x_i} \, d\alpha \tag{1}$$

Both generative approaches also admit a natural extension to Expected Gradients (EG) [16] by constructing a distribution of diverse yet semantically consistent counterfactual baselines. For the VAE-based approach, this is achieved by sampling perturbations around the optimized latent code z^*, e.g. $z \sim \mathcal{N}(z^*(x),\, \sigma_\phi^2(x)\, I)$, and decoding each sample into a distinct counterfactual. For the diffusion-based approach, diversity is introduced by applying independent noise realizations at each denoising step using a stochastic DDIM sampler with $\eta = 0.3$, yielding a set of varied yet plausible healthy reconstructions. In both cases, the EG attribution is:

$$\text{EG}(\text{CF})_i(x) = \mathbb{E}_{\hat{\text{CF}} \sim p_{\text{CF}}(x)} \left[(x_i - \hat{\text{CF}}_i) \int_{\alpha=0}^{1} \frac{\partial \mathcal{C}\left(\hat{\text{CF}} + \alpha \cdot (x - \hat{\text{CF}}_i)\right)}{\partial x_i} \, d\alpha \right] \tag{2}$$

where $p_{\text{CF}}(x)$ denotes the distribution over counterfactual baselines induced by either the VAE latent perturbations or the diffusion noise realizations.

4 Evaluation

Table 1: Description of compared baselines

Baseline	Description
Zeros	Tensor of zeros
Blurred	Blurred input using gaussian filter ($\sigma = 20$)
Uniform	Random noise input, where each pixel drawn from Uniform distribution
Ones	Tensor of ones (as counterpart to Zeros)
EG	Expected Gradients using a set of 50 randomly drawn training samples as baselines
CF$_{\text{Dif.}}$	The Diffusion-generated counterfactual representing the normal case
EG (CF)$_{\text{Dif.}}$	Expected Gradients using a set of 50 Diffusion-generated counterfactuals
CF$_{\text{VAE}}$	The VAE-generated counterfactual representing the normal case
EG (CF)$_{\text{VAE}}$	Expected Gradients using a set of 50 VAE-generated counterfactuals

Evaluating explainability methods, especially attribution maps, is challenging, as it is often unclear whether observed errors stem from the model or the attribution technique itself, prompting the identification of key limitations and the development of various evaluation strategies in recent years [12, 2, 22, 1, 48, 27, 26, 29, 37, 24].

To evaluate our proposed counterfactual-based baseline approaches, we compare them against standard baseline choices on three diverse medical data sets. Using multiple metrics, we demonstrate that our method constantly produces the most informative attributions by better highlighting the most relevant pixels. A detailed overview of the compared baseline choices is provided in Table 1. All experiments were implemented in PyTorch and conducted on a single NVIDIA L40S GPU.

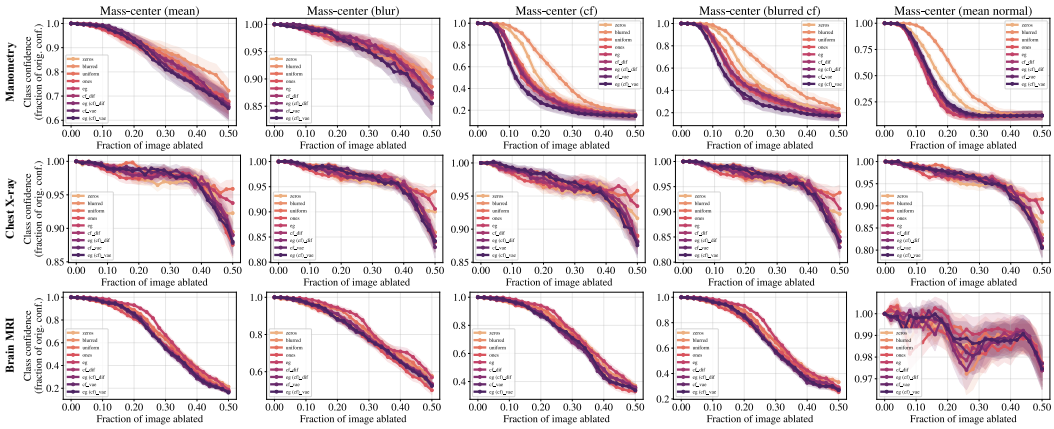


Figure 4: Mass-center ablation test results on the three data sets, where a lower curve indicates a better attribution. Results are aggregated (mean $\pm$ se) over all test samples.

Data sets We evaluate the baselines on three medical data sets: manometry, chest X-ray, brain MRI. The data sets contain class labels and segmentation masks for pathological region localization. Images are resized to 512×512 and normalized to $[0, 1]$. Evaluation is based on pathological test samples with available segmentation masks. Dataset details, splits, and sample sizes are described in appendix I. For a qualitative impression, Fig. 3 shows an example input from each data set with corresponding attribution maps for the various baselines we compare.

4.1 Metrics

We use multiple metrics to evaluate the performance of the different baselines. Before evaluating, the attributions are capped at the 99.9th percentile to avoid outlying high-intensity attributions to dominate the visualizations and evaluations.

Ablation tests An intuitive way to assess attribution quality are ablation tests, where certain pixels are replaced and the drop in classifier confidence is measured to assess their influence on the model output. In our experiments, we perform two common kinds of ablation tests [42, 18]: (1) Top-k ablation by removing the top-k most important pixels (provided by the different baselines) and measuring the drop in classifier confidence. (2) Region-based ablation by computing the attribution map's center of mass and ablating increasingly large square regions around it, testing for coherent, clinically relevant localization. We use two standard imputation methods to impute ablated pixels [42]: *Mean Imputation*: replace each pixel with image-wide mean; *Gaussian Blur*: replace each pixel with a blurred version. As these suffer from the same challenge when missingness is diagnostically meaningful, we additionally introduce the following more medically grounded imputations: *Counterfactual Imputation*: replace with corresponding pixel from generated healthy counterfactual; *Blurred Counterfactual Imputation*: replace with corresponding pixel from blurred counterfactual; *Mean Normal Imputation*: replace with pixelwise average from healthy training samples. We track how classifier confidence changes as more pixels are ablated. Faster confidence drops (i.e., lower curves) indicate more informative attributions.

Overlap of attributions with ground truth segmentation mask Attribution maps should align with regions of interest, making their overlap with ground truth segmentation masks a meaningful measure of plausibility [12, 9, 25]. To measure the overlap, we treat the attribution maps as predictions and the binary segmentation masks as targets. We then compute both the Precision-Recall AUC (PR-AUC) as well as the Mean Squared Error (MSE) as two measures of alignment. In addition, to assess attribution noise outside the relevant region, we measure the false positive attribution rate (FPAR), where a lower FPAR indicates a more focused and less noisy attribution map (highlighting fewer non-relevant regions). To measure this rate, we calculate the ratio of the sum of attributions outside the true mask to the sum of all attributions, formally $\text{FPAR} = \frac{\sum_{i,j} A_{i,j} \cdot (1 - M_{i,j})}{\sum_{i,j} A_{i,j}}$, with $A \in [0, 1]^{H \times W}$ being the attribution map, and $M \in \{0, 1\}^{H \times W}$ being the binary mask.

Table 2: Aggregated scores (mean ± se) measuring the overlap between attribution map and ground truth mask; $p < 0.01$ (*); The **best** and three next best scores are highlighted.

	Manometry			Chest X-ray			Brain MRI		
Baseline	MSE ↓ $(\cdot 10^{-2})$	PR-AUC ↑	FPAR ↓	MSE ↓ $(\cdot 10^{-2})$	PR-AUC ↑	FPAR ↓	MSE ↓ $(\cdot 10^{-2})$	PR-AUC ↑	FPAR ↓
Zeros	4.50 ± 0.29	0.19 ± 0.02	0.85 ± 0.01	1.52 ± 0.07	0.12 ± 0.01	0.92 ± 0.00	2.51 ± 0.12	0.39 ± 0.01	0.65 ± 0.01
Blurred	4.80 ± 0.30	0.12 ± 0.01	0.89 ± 0.01	1.33 ± 0.08	0.14 ± 0.01	**0.87 ± 0.01**	2.90 ± 0.12	0.21 ± 0.01	0.81 ± 0.01
Uniform	4.85 ± 0.29	0.09 ± 0.01	0.92 ± 0.01	1.59 ± 0.07	0.07 ± 0.00	0.94 ± 0.00	2.80 ± 0.12	0.21 ± 0.00	0.82 ± 0.00
Ones	4.55 ± 0.29	0.15 ± 0.01	0.88 ± 0.01	1.36 ± 0.07	**0.15 ± 0.01**	0.90 ± 0.01	2.91 ± 0.12	0.21 ± 0.01	0.84 ± 0.00
EG	4.45 ± 0.25	0.22 ± 0.02	0.83 ± 0.02	1.47 ± 0.06	0.12 ± 0.01	0.92 ± 0.01	2.59 ± 0.11	0.35 ± 0.01	0.75 ± 0.01
$\text{CF}_{\text{Dif.}}$	4.37 ± 0.29	0.23 ± 0.01	0.77 ± 0.02	1.33 ± 0.07	0.14 ± 0.01	**0.87 ± 0.01**	2.49 ± 0.12	0.43 ± 0.01	0.62 ± 0.01
$\text{EG (CF)}_{\text{Dif.}}$	4.26 ± 0.28	0.26 ± 0.01	0.77 ± 0.01	1.32 ± 0.07	0.14 ± 0.01	**0.87 ± 0.01**	2.48 ± 0.12	0.44 ± 0.01	0.62 ± 0.01
CF_{VAE}	**4.16 ± 0.31***	**0.32 ± 0.02***	**0.72 ± 0.02***	1.34 ± 0.07	0.13 ± 0.01	0.88 ± 0.01	2.45 ± 0.12	0.45 ± 0.01	**0.61 ± 0.01***
$\text{EG (CF)}_{\text{VAE}}$	4.17 ± 0.30	0.31 ± 0.02	0.74 ± 0.02	**1.31 ± 0.07**	0.14 ± 0.01	**0.87 ± 0.01**	**2.42 ± 0.12***	**0.46 ± 0.01***	0.62 ± 0.01

5 Results

Comparison to standard baselines The results of the mass-center ablation tests are shown in Fig. 4. Across all datasets, the proposed counterfactual baselines consistently achieve among the lowest curves, indicating stronger and more robust attribution performance than standard alternatives. This pattern holds regardless of baseline type or dataset, suggesting that the improvement stems from the principled satisfaction of semantic missingness rather than dataset-specific characteristics. Top-k ablation results, confirming similar trends, are provided in Appendix C.1.

The mask-overlap results demonstrate that the proposed counterfactual baselines consistently achieve the highest overlap scores across all datasets and metrics, as summarised in Table 2 (mean ± standard error). Statistical significance between the top-performing and next-best non-counterfactual baselines is assessed via paired t-tests or Wilcoxon tests, following normality testing of the differences. Our baselines outperform all alternatives across nearly every metric and dataset, with only Ones and Blurred performing comparably on the Chest X-ray dataset. Among the two proposed counterfactual approaches, the VAE-based counterfactuals tend to perform slightly better, likely due to classifier guidance during generation, which produces counterfactuals of higher quality.

These results indicate that counterfactual baselines produce more precise attribution maps with reduced noise outside regions of interest. This finding is consistent with our qualitative analysis, where the proposed baselines yield cleaner maps with fewer spurious attributions, as illustrated in Fig. 3 and Appendix C.2. Taken together, the quantitative and qualitative evidence demonstrates that counterfactual baselines generalise robustly across diverse datasets and evaluation criteria, whereas standard baselines exhibit greater variability and tend to perform well only in specific settings.

Comparison to pure counterfactual explanations Beyond their role as baselines, counterfactuals can also serve directly as explanations themselves, which is a separate explainability paradigm in its own. We take the difference $(x - \hat{\text{CF}})$ as the attribution map and then compare it to the attributions obtained with our proposed baseline approaches. While this raw difference can offer intuitive and visually informative insights, it lacks quantitative interpretability and its quality degrades rapidly when the counterfactual is imperfect, as the raw difference then captures spurious variation across the entire image rather than localizing to the pathologically relevant region. Using the counterfactual as a baseline for IG compensates for this by weighting feature contributions according to model sensitivity along the path, rather than pixel-wise distance alone. It also satisfies key axiomatic properties, which ensure theoretical soundness and consistence. A simple difference map does not guarantee those and therefore lacks the robustness required for reliable interpretability. This is reflected in our results: the absolute difference maps ($\text{DIFF}_{\text{Dif.}}$ and DIFF_{VAE}) in Table 3 perform significantly worse than the proposed baselines across all metrics, and the qualitative comparison in Fig. 5 shows that CF_{VAE} attributions concentrate precisely on the region

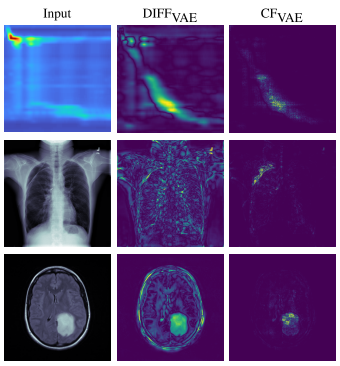


Figure 5: Comparison of the raw difference between the counterfactual and input (DIFF_{VAE}) vs. using IG with CF_{VAE} baseline

Table 3: Aggregated scores (mean ± se) comparing proposed baselines to related explainability approaches; $p < 0.01$ (*)

	Manometry			Chest X-ray			Brain MRI		
Baseline	MSE ↓ $(\cdot 10^{-2})$	PR-AUC ↑	FPAR ↓	MSE ↓ $(\cdot 10^{-2})$	PR-AUC ↑	FPAR ↓	MSE ↓ $(\cdot 10^{-2})$	PR-AUC ↑	FPAR ↓
$\text{DIFF}_{\text{Dif.}}$	5.87 ± 0.24	0.14 ± 0.01	0.91 ± 0.01	3.21 ± 0.09	0.03 ± 0.00	0.97 ± 0.00	4.28 ± 0.09	0.14 ± 0.01	0.90 ± 0.00
DIFF_{VAE}	5.88 ± 0.32	**0.33 ± 0.02**	0.87 ± 0.01	2.58 ± 0.08	0.03 ± 0.00	0.97 ± 0.00	4.22 ± 0.09	0.16 ± 0.01	0.89 ± 0.00
Mean (n)	4.46 ± 0.26	0.21 ± 0.02	0.81 ± 0.01	1.44 ± 0.07	0.11 ± 0.01	0.91 ± 0.01	2.95 ± 0.12	0.18 ± 0.01	0.83 ± 0.01
Rand (n)	4.57 ± 0.28	0.18 ± 0.02	0.83 ± 0.01	1.60 ± 0.07	0.07 ± 0.01	0.94 ± 0.00	2.70 ± 0.12	0.28 ± 0.01	0.75 ± 0.01
EG (n)	4.40 ± 0.25	0.24 ± 0.02	0.82 ± 0.01	1.48 ± 0.07	0.12 ± 0.01	0.92 ± 0.00	2.54 ± 0.11	0.37 ± 0.01	0.74 ± 0.01
LIG [14]	4.37 ± 0.29	0.24 ± 0.02	0.80 ± 0.02	1.52 ± 0.07	0.04 ± 0.00	0.96 ± 0.00	3.09 ± 0.12	0.15 ± 0.01	0.84 ± 0.01
CF-IG [15]	4.43 ± 0.28	0.20 ± 0.01	0.81 ± 0.01	1.43 ± 0.07	0.12 ± 0.01	0.90 ± 0.01	2.72 ± 0.13	0.31 ± 0.01	0.72 ± 0.01
GIG [25]	4.50 ± 0.29	0.19 ± 0.02	0.85 ± 0.01	1.52 ± 0.06	0.12 ± 0.01	0.92 ± 0.01	2.51 ± 0.12	0.39 ± 0.01	0.65 ± 0.01
IG2 [51]	4.76 ± 0.30	0.11 ± 0.01	0.88 ± 0.01	1.55 ± 0.08	0.04 ± 0.00	0.96 ± 0.00	3.17 ± 0.13	0.07 ± 0.00	0.91 ± 0.00
$\text{CF}_{\text{Dif.}}$	4.37 ± 0.29	0.23 ± 0.01	0.77 ± 0.02	1.33 ± 0.07	**0.14 ± 0.01**	**0.87 ± 0.01**	2.49 ± 0.12	0.43 ± 0.01	0.62 ± 0.01
$\text{EG (CF)}_{\text{Dif.}}$	4.26 ± 0.28	0.26 ± 0.01	0.77 ± 0.01	1.32 ± 0.07	**0.14 ± 0.01**	**0.87 ± 0.01**	2.48 ± 0.12	0.44 ± 0.01	0.62 ± 0.01
CF_{VAE}	**4.16 ± 0.31***	0.32 ± 0.02	**0.72 ± 0.02***	1.34 ± 0.07	0.13 ± 0.01	0.88 ± 0.01	2.45 ± 0.12	0.45 ± 0.01	**0.61 ± 0.01***
$\text{EG (CF)}_{\text{VAE}}$	4.17 ± 0.30	0.31 ± 0.02	0.74 ± 0.02	**1.31 ± 0.07***	**0.14 ± 0.01**	**0.87 ± 0.01***	**2.42 ± 0.12***	**0.46 ± 0.01***	0.62 ± 0.01

of interest while DIFF_{VAE} highlights diffuse regions throughout the image. These findings reinforce the value of counterfactuals as principled baselines for IG over their use as standalone explanations. An extended discussion, ablation tests, and additional qualitative results are provided in Appendix D.

Comparison to related concepts Since our approach is conceptually distinct, yet grounded in similar underlying principles, we compare it to LIG [14] and CF-IG [15], as well as to the adaptive path methods GIG [25], and IG2 [51]. Additionally, our analysis also concerns the necessity of generating a dedicated counterfactual for each input, as an alternative and potentially simpler strategy might be to use samples from the normal class as baselines for IG. To investigate this, we additionally evaluate three baseline strategies that sample directly from the normal class in the training set: Mean (n): the mean of all normal samples; Rand (n): a single random normal sample; EG (n): EG with 50 random normal samples.

The results, reported in Table 3, show that counterfactual baselines consistently outperform the related concepts and alternative baselines, emphasizing the necessity of an input-specific baseline. Additional ablation tests, as well as qualitative results and implementation details are provided in Appendix E.

6 Conclusion

In this work we analyze counterfactual baselines for path attribution methods. Driven by the limitations of standard baselines, we introduce *semantic missingness* as a stricter requirement for baselines in medical settings, which in turn motivates clinically "normal" counterfactuals as a more meaningful baseline choice. Through both theoretical analysis and extensive experiments across three medical datasets, we show that counterfactual baselines yield more faithful, localized, and clinically relevant attributions than conventional alternatives and related methods. Moreover, we show that using counterfactuals as baselines for IG outperforms using them directly as explanations, bridging two complementary explainability paradigms.

Broader impact By challenging the assumption that conventional baselines adequately represent missing information, our work contributes to the safer and more responsible deployment of explainable AI in healthcare. Attribution maps aim to increase transparency, but can mislead clinicians if not faithfully generated. Improving their quality reduces this risk and helps practitioners better understand model decisions. Beyond healthcare, our model-agnostic framework provides a general strategy for domain-aware explanations applicable to other safety-critical settings.

Limitations While our approach improves attribution faithfulness across the evaluated settings, it has certain limitations (mostly related to additional compute), which we discuss in detail in appendix F.

Future work Being model-agnostic, our framework can be paired with more advanced generative models to further improve counterfactual fidelity and, in turn, attribution quality. Stronger classifiers may likewise enhance the trustworthiness of the resulting explanations, and ensembling counterfactual and conventional baselines could yield additional gains in robustness. Together, these directions point toward more transparent, trustworthy, and clinically meaningful explainability in medical AI.

References

[1] Julius Adebayo, Justin Gilmer, Michael Muelly, Ian Goodfellow, Moritz Hardt, and Been Kim. Sanity Checks for Saliency Maps. In *Advances in Neural Information Processing Systems*, volume 31. Curran Associates, Inc., 2018.

[2] Marco Ancona, Enea Ceolini, Cengiz Öztireli, and Markus Gross. Towards better understanding of gradient-based attribution methods for Deep Neural Networks. In *6th International Conference on Learning Representations, ICLR 2018*, 2018. doi: 10.3929/ethz-b-000249929.

[3] Plamen P. Angelov, Eduardo A. Soares, Richard Jiang, Nicholas I. Arnold, and Peter M. Atkinson. Explainable artificial intelligence: An analytical review. *WIREs Data Mining and Knowledge Discovery*, 11(5):e1424, 2021. doi: 10.1002/widm.1424.

[4] Matan Atad, David Schinz, Hendrik Moeller, Robert Graf, Benedikt Wiestler, Daniel Rueckert, Nassir Navab, Jan S. Kirschke, and Matthias Keicher. Counterfactual Explanations for Medical Image Classification and Regression using Diffusion Autoencoder. *Machine Learning for Biomedical Imaging*, 2(iMIMIC 2023 special issue):2103–2125, September 2024. doi: 10.59275/j.melba.2024-4862.

[5] Cher Bass, Mariana da Silva, Carole Sudre, Petru-Daniel Tudosiu, Stephen Smith, and Emma Robinson. ICAM: Interpretable Classification via Disentangled Representations and Feature Attribution Mapping. In *Advances in Neural Information Processing Systems*, volume 33, pages 7697–7709. Curran Associates, Inc., 2020.

[6] Christian F. Baumgartner, Lisa M. Koch, Kerem Can Tezcan, Jia Xi Ang, and Ender Konukoglu. Visual Feature Attribution Using Wasserstein GANs. In *2018 IEEE/CVF Conference on Computer Vision and Pattern Recognition*, pages 8309–8319, Salt Lake City, UT, USA, June 2018. IEEE. ISBN 978-1-5386-6420-9. doi: 10.1109/CVPR.2018.00867.

[7] Johanna M. Brandenburg, Beat P. Müller-Stich, Martin Wagner, and Mihaela van der Schaar. Can surgeons trust AI? Perspectives on machine learning in surgery and the importance of eXplainable Artificial Intelligence (XAI). *Langenbeck's Archives of Surgery*, 410(1), 2025. doi: 10.1007/s00423-025-03626-7.

[8] Mateusz Buda, Ashirbani Saha, and Maciej Mazurowski. Association of genomic subtypes of lower-grade gliomas with shape features automatically extracted by a deep learning algorithm. *Computers in Biology and Medicine*, 109, May 2019. doi: 10.1016/j.compbiomed.2019.05.002.

[9] Zoya Bylinskii, Tilke Judd, Aude Oliva, Antonio Torralba, and Fredo Durand. What Do Different Evaluation Metrics Tell Us About Saliency Models? *IEEE Transactions on Pattern Analysis and Machine Intelligence*, 41(3):740–757, March 2019. doi: 10.1109/TPAMI.2018.2815601.

[10] Ahmad Chaddad, Jihao Peng, Jian Xu, and Ahmed Bouridane. Survey of Explainable AI Techniques in Healthcare. *Sensors*, 23(2):634, January 2023. doi: 10.3390/s23020634.

[11] James R. Clough, Ilkay Oksuz, Esther Puyol-Antón, Bram Ruijsink, Andrew P. King, and Julia A. Schnabel. Global and Local Interpretability for Cardiac MRI Classification. In Dinggang Shen, Tianming Liu, Terry M. Peters, Lawrence H. Staib, Caroline Essert, Sean Zhou, Pew-Thian Yap, and Ali Khan, editors, *Medical Image Computing and Computer Assisted Intervention – MICCAI 2019*, pages 656–664, Cham, 2019. Springer International Publishing. ISBN 978-3-030-32251-9. doi: 10.1007/978-3-030-32251-9_72.

[12] Piotr Dabkowski and Yarin Gal. Real Time Image Saliency for Black Box Classifiers. In *Advances in Neural Information Processing Systems*, volume 30. Curran Associates, Inc., 2017.

[13] Maxime Di Folco, Cosmin I. Bercea, Emily Chan, and Julia A. Schnabel. Interpretable Representation Learning of Cardiac MRI via Attribute Regularization. In Marius George Linguraru, Qi Dou, Aasa Feragen, Stamatia Giannarou, Ben Glocker, Karim Lekadir, and Julia A. Schnabel, editors, *Medical Image Computing and Computer Assisted Intervention – MICCAI 2024*, pages 492–501, Cham, 2024. Springer Nature Switzerland. ISBN 978-3-031-72117-5. doi: 10.1007/978-3-031-72117-5_46.

[14] Amil Dravid, Florian Schiffers, Boqing Gong, and Aggelos K. Katsaggelos. medXGAN: Visual Explanations for Medical Classifiers through a Generative Latent Space. In *2022 IEEE/CVF Conference on Computer Vision and Pattern Recognition Workshops (CVPRW)*, pages 2935–2944, New Orleans, LA, USA, June 2022. IEEE. ISBN 978-1-6654-8739-9. doi: 10.1109/CVPRW56347.2022.00331.

[15] Jamie Duell, Monika Seisenberger, and Xiuyi Fan. Counterfactual-Integrated Gradients: Counterfactual Feature Attribution for Medical Records. In *2023 IEEE International Conference on Bioinformatics and Biomedicine*, December 2023. doi: 10.1109/BIBM58861.2023.10385466.

[16] Gabriel Erion, Joseph D. Janizek, Pascal Sturmfels, Scott M. Lundberg, and Su-In Lee. Improving performance of deep learning models with axiomatic attribution priors and expected gradients. *Nature Machine Intelligence*, 3(7):620–631, July 2021. doi: 10.1038/s42256-021-00343-w.

[17] Ruth C. Fong and Andrea Vedaldi. Interpretable Explanations of Black Boxes by Meaningful Perturbation. In *2017 IEEE International Conference on Computer Vision (ICCV)*, pages 3449–3457, Venice, October 2017. IEEE. ISBN 978-1-5386-1032-9. doi: 10.1109/ICCV.2017.371.

[18] Amirata Ghorbani, Abubakar Abid, and James Zou. Interpretation of Neural Networks Is Fragile. *Proceedings of the AAAI Conference on Artificial Intelligence*, 33(01):3681–3688, July 2019. doi: 10.1609/aaai.v33i01.33013681.

[19] Victor Guyomard, Françoise Fessant, Thomas Guyet, Alexandre termier, and Tassadit Bouadi. VCNet: A self-explaining model for realistic counterfactual generation. In *Machine Learning and Knowledge Discovery in Databases - European Conference, ECML PKDD 2022, Grenoble, France, September 19-23, 2022, Proceedings, Part I*, September 2022.

[20] Jonathan Ho and Tim Salimans. Classifier-Free Diffusion Guidance, July 2022.

[21] Jonathan Ho, Ajay Jain, and Pieter Abbeel. Denoising Diffusion Probabilistic Models. In *Advances in Neural Information Processing Systems*, volume 33, pages 6840–6851. Curran Associates, Inc., 2020.

[22] Sara Hooker, Dumitru Erhan, Pieter-Jan Kindermans, and Been Kim. A Benchmark for Interpretability Methods in Deep Neural Networks. In *Advances in Neural Information Processing Systems*, volume 32. Curran Associates, Inc., 2019.

[23] Md Imran Hossain, Ghada Zamzmi, Peter R. Mouton, Md Sirajus Salekin, Yu Sun, and Dmitry Goldgof. Explainable AI for Medical Data: Current Methods, Limitations, and Future Directions. *ACM Computing Surveys*, 57(6):1–46, June 2025. doi: 10.1145/3637487.

[24] Md Abdul Kadir, Amir Mosavi, and Daniel Sonntag. Evaluation Metrics for XAI: A Review, Taxonomy, and Practical Applications. In *2023 IEEE 27th International Conference on Intelligent Engineering Systems (INES)*, pages 000111–000124, Nairobi, Kenya, July 2023. IEEE. ISBN 979-8-3503-2851-6. doi: 10.1109/INES59282.2023.10297629.

[25] Andrei Kapishnikov, Subhashini Venugopalan, Besim Avci, Ben Wedin, Michael Terry, and Tolga Bolukbasi. Guided Integrated Gradients: An Adaptive Path Method for Removing Noise. In *2021 IEEE/CVF Conference on Computer Vision and Pattern Recognition (CVPR)*, pages 5048–5056, Nashville, TN, USA, June 2021. IEEE. ISBN 978-1-6654-4509-2. doi: 10.1109/CVPR46437.2021.00501.

[26] Sunnie S. Y. Kim, Nicole Meister, Vikram V. Ramaswamy, Ruth Fong, and Olga Russakovsky. HIVE: Evaluating the Human Interpretability of Visual Explanations. In Shai Avidan, Gabriel Brostow, Moustapha Cissé, Giovanni Maria Farinella, and Tal Hassner, editors, *Computer Vision – ECCV 2022*, pages 280–298, Cham, 2022. Springer Nature Switzerland. ISBN 978-3-031-19775-8. doi: 10.1007/978-3-031-19775-8_17.

[27] Pieter-Jan Kindermans, Sara Hooker, Julius Adebayo, Maximilian Alber, Kristof T. Schütt, Sven Dähne, Dumitru Erhan, and Been Kim. The (Un)reliability of Saliency Methods. In Wojciech Samek, Grégoire Montavon, Andrea Vedaldi, Lars Kai Hansen, and Klaus-Robert Müller, editors, *Explainable AI: Interpreting, Explaining and Visualizing Deep Learning*, pages 267–280. Springer International Publishing, Cham, 2019. ISBN 978-3-030-28954-6. doi: 10.1007/978-3-030-28954-6_14.

[28] Diederik P. Kingma and Max Welling. Auto-Encoding Variational Bayes. In *2nd International Conference on Learning Representations, ICLR 2014, Banff, AB, Canada, April 14-16, 2014, Conference Track Proceedings*, 2014.

[29] Isaac Lage, Emily Chen, Jeffrey He, Menaka Narayanan, Been Kim, Sam Gershman, and Finale Doshi-Velez. An Evaluation of the Human-Interpretability of Explanation, August 2019.

[30] Ze Liu, Han Hu, Yutong Lin, Zhuliang Yao, Zhenda Xie, Yixuan Wei, Jia Ning, Yue Cao, Zheng Zhang, Li Dong, Furu Wei, and Baining Guo. Swin Transformer V2: Scaling Up Capacity and Resolution. In *2022 IEEE/CVF Conference on Computer Vision and Pattern Recognition (CVPR)*, pages 11999–12009, June 2022. doi: 10.1109/CVPR52688.2022.01170.

[31] Scott M. Lundberg and Su-In Lee. A unified approach to interpreting model predictions. In *Proceedings of the 31st International Conference on Neural Information Processing Systems*, NIPS'17, pages 4768–4777, Red Hook, NY, USA, December 2017. Curran Associates Inc. ISBN 978-1-5108-6096-4.

[32] Daniel D. Lundstrom, Tianjian Huang, and Meisam Razaviyayn. A Rigorous Study of Integrated Gradients Method and Extensions to Internal Neuron Attributions. In *Proceedings of the 39th International Conference on Machine Learning*, pages 14485–14508. PMLR, June 2022.

[33] Silvan Mertes, Tobias Huber, Katharina Weitz, Alexander Heimerl, and Elisabeth André. GANterfactual—Counterfactual Explanations for Medical Non-experts Using Generative Adversarial Learning. *Frontiers in Artificial Intelligence*, 5, April 2022. doi: 10.3389/frai.2022.825565.

[34] Dang Minh, H. Xiang Wang, Y. Fen Li, and Tan N. Nguyen. Explainable artificial intelligence: A comprehensive review. *Artificial Intelligence Review*, 55(5):3503–3568, June 2022. doi: 10.1007/s10462-021-10088-y.

[35] Ramaravind K. Mothilal, Amit Sharma, and Chenhao Tan. Explaining machine learning classifiers through diverse counterfactual explanations. In *Proceedings of the 2020 Conference on Fairness, Accountability, and Transparency*, FAT* '20, pages 607–617, New York, NY, USA, January 2020. Association for Computing Machinery. ISBN 978-1-4503-6936-7. doi: 10.1145/3351095.3372850.

[36] Supriya Nagesh, Nina Mishra, Yonatan Naamad, James M. Rehg, Mehul A. Shah, and Alexei Wagner. Explaining a machine learning decision to physicians via counterfactuals. In *Proceedings of the Conference on Health, Inference, and Learning*, pages 556–577. PMLR, June 2023.

[37] Menaka Narayanan, Emily Chen, Jeffrey He, Been Kim, Sam Gershman, and Finale Doshi-Velez. How do Humans Understand Explanations from Machine Learning Systems? An Evaluation of the Human-Interpretability of Explanation, February 2018.

[38] Paraskevas Pegios, Aasa Feragen, Andreas Abildtrup Hansen, and Georgios Arvanitidis. Counterfactual Explanations via Riemannian Latent Space Traversal, November 2024.

[39] Kathryn Schutte, Olivier Moindrot, Paul Hérent, Jean-Baptiste Schiratti, and Simon Jégou. Using StyleGAN for Visual Interpretability of Deep Learning Models on Medical Images, January 2021.

[40] Avanti Shrikumar, Peyton Greenside, and Anshul Kundaje. Learning Important Features Through Propagating Activation Differences. In *Proceedings of the 34th International Conference on Machine Learning*, pages 3145–3153. PMLR, July 2017.

[41] Jiaming Song, Chenlin Meng, and Stefano Ermon. Denoising Diffusion Implicit Models. In *International Conference on Learning Representations*, October 2020.

[42] Pascal Sturmfels, Scott Lundberg, and Su-In Lee. Visualizing the Impact of Feature Attribution Baselines. *Distill*, 5(1):e22, January 2020. doi: 10.23915/distill.00022.

[43] Qiyang Sun, Alican Akman, and Björn W. Schuller. Explainable Artificial Intelligence for Medical Applications: A Review. *ACM Transactions on Computing for Healthcare*, 6(2):1–31, April 2025. doi: 10.1145/3709367.

[44] Mukund Sundararajan, Ankur Taly, and Qiqi Yan. Axiomatic Attribution for Deep Networks. In *Proceedings of the 34th International Conference on Machine Learning*, pages 3319–3328. PMLR, July 2017.

[45] Toygar Tanyel, Serkan Ayvaz, and Bilgin Keserci. Beyond Known Reality: Exploiting Counterfactual Explanations for Medical Research, February 2025.

[46] Bas H. M. van der Velden, Hugo J. Kuijf, Kenneth G. A. Gilhuijs, and Max A. Viergever. Explainable artificial intelligence (XAI) in deep learning-based medical image analysis. *Medical Image Analysis*, 79:102470, July 2022. doi: 10.1016/j.media.2022.102470.

[47] Nina Weng, Paraskevas Pegios, Eike Petersen, Aasa Feragen, and Siavash Bigdeli. Fast Diffusion-Based Counterfactuals for Shortcut Removal and Generation. In Aleš Leonardis, Elisa Ricci, Stefan Roth, Olga Russakovsky, Torsten Sattler, and Gül Varol, editors, *European Conference on Computer Vision*, volume 15144, pages 338–357, Cham, 2025. Springer Nature Switzerland. ISBN 978-3-031-73015-3 978-3-031-73016-0. doi: 10.1007/978-3-031-73016-0_20.

[48] Chih-Kuan Yeh, Cheng-Yu Hsieh, Arun Suggala, David I Inouye, and Pradeep K Ravikumar. On the (In)fidelity and Sensitivity of Explanations. In *Advances in Neural Information Processing Systems*, volume 32. Curran Associates, Inc., 2019.

[49] Eslam Zaher, Maciej Trzaskowski, Quan Nguyen, and Fred Roosta. Manifold integrated gradients: Riemannian geometry for feature attribution. In *Proceedings of the 41st International Conference on Machine Learning*, volume 235 of *ICML'24*, pages 58090–58104, Vienna, Austria, July 2024. JMLR.org.

[50] Anna Zawacki, Carol Wu, George Shih, Julia Elliott, Mikhail Fomitchev, Mohannad Hussain, ParasLakhani, Phil Culliton, and Shunxing Bao. Siim-acr pneumothorax segmentation, 2019. Kaggle.

[51] Yue Zhuo and Zhiqiang Ge. IG2: Integrated Gradient on Iterative Gradient Path for Feature Attribution. *IEEE Transactions on Pattern Analysis and Machine Intelligence*, 46(11):7173–7190, November 2024. doi: 10.1109/TPAMI.2024.3388092.

Appendix

A Theoretical analysis - Proofs **15**
A.1 Perfect Counterfactual Baseline 15
A.2 Approximate counterfactuals 15

B Empirical Validation of the Counterfactual Proximity Effect **17**

C Additional results - Comparison to standard baselines **18**
C.1 Top-k ablations 18
C.2 Examples for qualitative evaluation 18

D Comparison to pure counterfactual explanations - Using difference between input and counterfactual directly as the explanation **20**

E Comparison to other baseline choices, related works, and why a counterfactual is needed **23**

F Limitations **26**

G Quantitative assessment of realism of generated counterfactuals **27**

H Dynamic counterfactual baseline generation **29**
H.1 Dynamic counterfactual baseline generation using VAEs 29
H.2 Dynamic counterfactual baseline generation using diffusion models 30

I Details of data sets **32**

J Analysis of computational cost **33**

K Model descriptions **34**
K.1 Diffusion model 34
K.2 VAE 34
K.3 Classifier 35

A Theoretical analysis - Proofs

Preliminaries Let $\mathcal{C} : \mathbb{R}^d \to \mathbb{R}$ denote a continuously differentiable model (e.g., a class logit). For an input $x \in \mathbb{R}^d$ and a baseline $b \in \mathbb{R}^d$, the path-integrated gradient vector can be defined as

$$A(b) := \int_0^1 \nabla \mathcal{C}\big(b + \alpha(x - b)\big)\, d\alpha. \tag{3}$$

Then IG can be written compactly using the Hadamard (elementwise) product $\circ$:

$$\mathrm{IG}(x; b) = (x - b) \circ A(b). \tag{4}$$

Integrated Gradients satisfies the *completeness* property:

$$\sum_{i=1}^{d} \mathrm{IG}_i(x; b) = \mathcal{C}(x) - \mathcal{C}(b). \tag{5}$$

A.1 Perfect Counterfactual Baseline

Let $\mathcal{C} : \mathbb{R}^n \to \mathbb{R}$ be a differentiable function representing the scalar prediction of interest (e.g., the logit for a disease class). Let $x \in \mathbb{R}^n$ be a fixed input and let $S \subseteq \{1, \ldots, n\}$ denote the (unknown) set of *pathological coordinates*, i.e., the coordinates where the input differs from a corresponding healthy, pathology-free version.

Definition A.1 (Perfect Counterfactual Baseline)**.** A baseline $\mathrm{CF}^* \in \mathbb{R}^n$ is called a *perfect counterfactual baseline* if $\mathcal{C}(\mathrm{CF}^*)$ corresponds to a neutral prediction, there exists a minimal causal index set $S \subseteq \{1, \ldots, n\}$ such that $x_i = \mathrm{CF}^*_i$ for all $i \notin S$;, and the prediction difference $\mathcal{C}(x) - \mathcal{C}(\mathrm{CF}^*)$ depends only on coordinates in S.

Intuitively, x^{cf} differs from x only in those features causally responsible for the prediction. In this case, we can show that all attribution mass is concentrated on the causal coordinates S only.

Proposition 3 (Perfect Attribution under Perfect Counterfactual Baseline)**.** Let $\mathcal{C}$ be continuously differentiable and let CF^* be a perfect counterfactual baseline for x. Then (1) $\mathrm{IG}_i(x; \mathrm{CF}^*) = 0$ for all $i \notin S$ and (2) $\sum_{i \in S} \mathrm{IG}_i(x; \mathrm{CF}^*) = \mathcal{C}(x) - \mathcal{C}(\mathrm{CF}^*)$.

Proof. For any coordinate $i \notin S$, we have $x_i = x_i^{cf}$. By definition of IG,

$$\mathrm{IG}_i(x; x^{cf}) = (x_i - x_i^{cf}) \int_0^1 \frac{\partial \mathcal{C}(x^{cf} + \alpha(x - x^{cf}))}{\partial x_i}\, d\alpha. \tag{6}$$

Since $x_i - x_i^{cf} = 0$, it follows that

$$\mathrm{IG}_i(x; x^{cf}) = 0. \tag{7}$$

By completeness,

$$\sum_{i=1}^{d} \mathrm{IG}_i(x; x^{cf}) = \mathcal{C}(x) - \mathcal{C}(x^{cf}). \tag{8}$$

Because only coordinates in S differ between x and x^{cf}, and all other coordinates receive zero attribution, we obtain

$$\sum_{i \in S} \mathrm{IG}_i(x; x^{cf}) = \mathcal{C}(x) - \mathcal{C}(x^{cf}). \tag{9}$$

Thus all attribution mass is concentrated on S. □

A.2 Approximate counterfactuals

In practice, a perfect counterfactual may not be available. We therefore consider approximate counterfactual baselines. For our theoretical analysis, we will make the following assumptions.

Note 1 (Assumptions). We assume

(A1) (**Lipschitz gradient**) $\nabla \mathcal{C}$ is L-Lipschitz on the convex hull of $\{x, x^{cf}, b\}$:

$$\|\nabla \mathcal{C}(u) - \nabla \mathcal{C}(v)\|_2 \leq L\|u - v\|_2.$$

(A2) (**Bounded gradients**) There exists $G_\infty < \infty$ such that along the integration paths

$$\|\nabla \mathcal{C}(z)\|_\infty \leq G_\infty.$$

We show that, under these assumptions, if an approximate counterfactual baseline $\tilde{x}$ is closer to the perfect counterfactual $x^\star$ than a standard baseline b is, then the corresponding attribution $\mathrm{IG}(x; \tilde{x})$ is closer to the ideal attribution $\mathrm{IG}(x; x^\star)$ in terms of error upper bound than $\mathrm{IG}(x; b)$ is.

Proposition 4 (Closeness to True Counterfactual Implies Lower Attribution Error Upper Bound). Let $b \in \mathbb{R}^d$ be an arbitrary baseline. Define $\delta_b := \|b - \mathrm{CF}^*\|_2$ and $C := \frac{L}{2}\|x - \mathrm{CF}^*\|_2 + G_\infty$. Under assumptions (A1) and (A2), for any baseline b,

$$\|\mathrm{IG}(x; b) - \mathrm{IG}(x; \mathrm{CF}^*)\|_2 \leq C\,\delta_b.$$

Consequently, for two baselines b_1, b_2, if $\|b_1 - \mathrm{CF}^*\|_2 < \|b_2 - \mathrm{CF}^*\|_2$, then their corresponding worst-case upper bounds satisfy $C\|b_1 - \mathrm{CF}^*\|_2 < C\|b_2 - \mathrm{CF}^*\|_2$. Hence, a baseline closer to the true counterfactual admits a strictly tighter theoretical upper bound on the attribution deviation.

Proof. Using the compact form $\mathrm{IG}(x; b) = (x - b) \circ A(b)$, we write

$$\mathrm{IG}(x; b) - \mathrm{IG}(x; x^{cf}) = (x - x^{cf}) \circ (A(b) - A(x^{cf})) \tag{10}$$

$$+ (x^{cf} - b) \circ A(b). \tag{11}$$

Step 1: Bounding $\mathbf{A(b) - A(x^{cf})}$. For $\alpha \in [0, 1]$, define

$$u(\alpha) = x^{cf} + \alpha(x - x^{cf}), \quad v(\alpha) = b + \alpha(x - b). \tag{12}$$

Then

$$u(\alpha) - v(\alpha) = (1 - \alpha)(x^{cf} - b), \tag{13}$$

so

$$\|u(\alpha) - v(\alpha)\|_2 = (1 - \alpha)\delta_b. \tag{14}$$

By the Lipschitz assumption,

$$\|\nabla \mathcal{C}(u(\alpha)) - \nabla \mathcal{C}(v(\alpha))\|_2 \leq L(1 - \alpha)\delta_b. \tag{15}$$

Integrating over α,

$$\|A(b) - A(x^{cf})\|_2 \leq \int_0^1 L(1 - \alpha)\delta_b \, d\alpha = \frac{L}{2}\delta_b. \tag{16}$$

Step 2: Bounding the two terms. Using $\|u \circ v\|_2 \leq \|u\|_2 \|v\|_\infty$:

$$\|(x - x^{cf}) \circ (A(b) - A(x^{cf}))\|_2 \leq \|x - x^{cf}\|_2 \|A(b) - A(x^{cf})\|_\infty \tag{17}$$

$$\leq \frac{L}{2}\|x - x^{cf}\|_2 \delta_b. \tag{18}$$

Similarly,

$$\|(x^{cf} - b) \circ A(b)\|_2 \leq \|x^{cf} - b\|_2 \|A(b)\|_\infty \tag{19}$$

$$\leq \delta_b G_\infty. \tag{20}$$

Combining the bounds.

$$\|\mathrm{IG}(x; b) - \mathrm{IG}(x; x^{cf})\|_2 \leq \left(\frac{L}{2}\|x - x^{cf}\|_2 + G_\infty\right)\delta_b = C\delta_b. \tag{21}$$

The comparison between the bounds of two baselines follows immediately. □

B Empirical Validation of the Counterfactual Proximity Effect

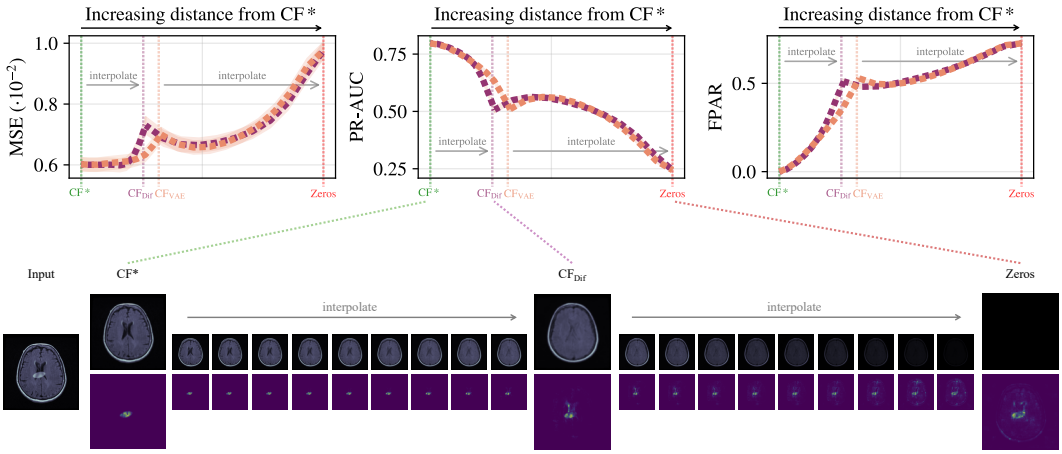


Figure 6: MSE, PR-AUC, and FPAR scores when increasing the distance to the perfect counterfactual CF^* by interpolating to the approximated counterfactual baselines and then interpolating to the zeros baseline.

To empirically assess how baseline distance from the true counterfactual affects attribution quality, we construct a controlled synthetic experiment based on the brain MRI dataset. Specifically, we take all healthy-class images and synthetically implant a tumor-shaped object into a randomly sampled half, yielding a binary classification task analogous to our other datasets. A classifier is then trained on this synthetic dataset following the same protocol.

The key advantage of this construction is that the unmodified healthy images serve as *exact* counterfactuals CF^*, i.e. they are the true disease-free counterparts of the pathological inputs, with no generative approximation involved. This allows us to precisely control and measure the distance between a given baseline and the oracle counterfactual.

We then design a baseline interpolation trajectory that spans from CF^* through our VAE- and diffusion-generated approximations and continues to the zero baseline, thereby constructing a continuum of baselines of increasing distance from the true counterfactual. Attribution quality metrics are computed at each point along this trajectory.

As shown in Fig. 6, attribution quality degrades gradually as the baseline moves further from CF^*. This provides direct empirical support for our theoretical result: increasing the distance between a baseline and the true counterfactual leads to a measurable and systematic decrease in attribution quality. Taken together, the synthetic experiment confirms that the gains observed with our counterfactual baselines are not incidental, but follow from a principled relationship between baseline proximity and attribution faithfulness.

C Additional results - Comparison to standard baselines

C.1 Top-k ablations

As described in section 4.1, we apply the top-k ablation test by removing the top-k percent of attributions and observe how the confidence of the classifier in the target class drops. Fig. 7 shows the results for the standard baselines and our proposed baseline approaches. It can be observed that for the Manometry data set it makes a bigger difference which imputation method is used, arguably due to the challenge of missingness in this data set. On the other two data sets, the ablation performances are comparable across baseline choices.

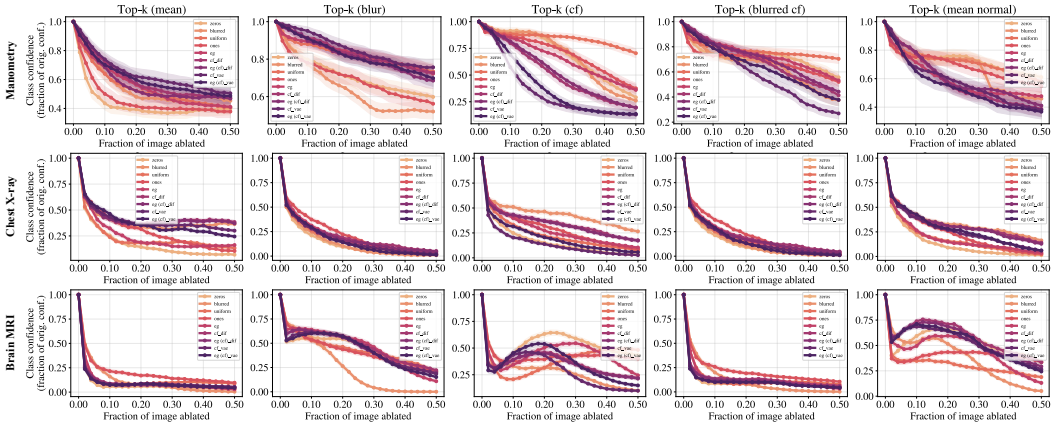
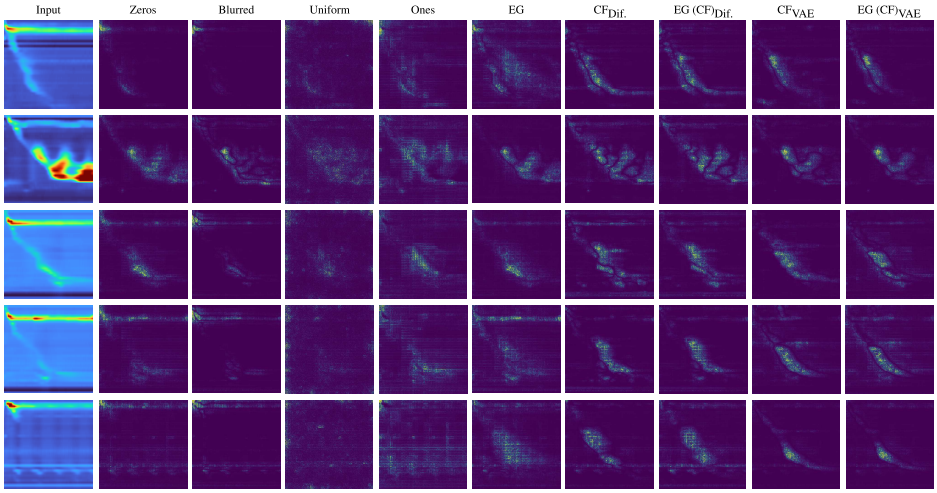


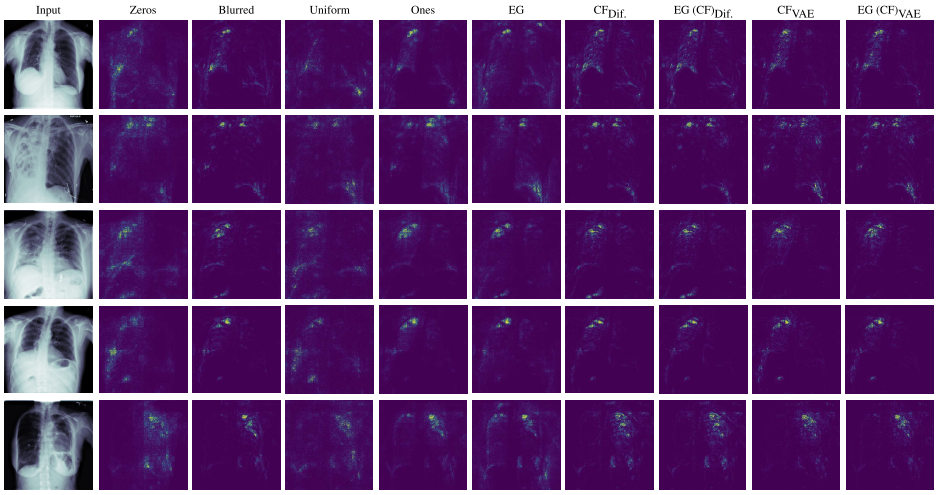
Figure 7: Results of the Top-k ablation tests

C.2 Examples for qualitative evaluation

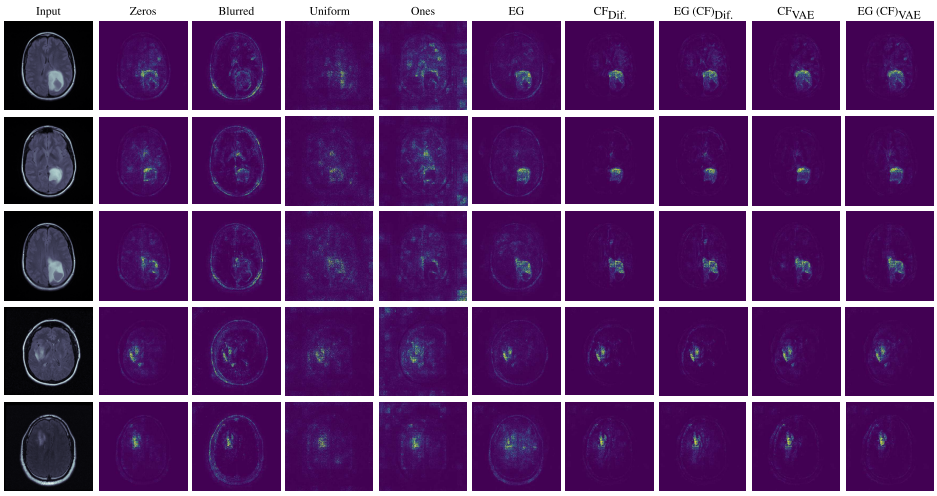
Fig. 8 contains more examples from each data set for a qualitative evaluation and comparison of the attributions obtained by the different baselines.



(a) Manometry



(b) Chest X-ray



(c) Brain MRI

Figure 8: Five examples from each data set for a qualitative comparison of the attributions obtained by the different baseline choices.

D Comparison to pure counterfactual explanations - Using difference between input and counterfactual directly as the explanation

Table 4: Aggregated scores (mean ± se) comparing proposed baselines to alternative approaches $\text{DIFF}_{\text{Dif.}}$ and DIFF_{VAE}; $p < 0.01$ (*)

	Manometry			Chest X-ray			Brain MRI		
Baseline	MSE ↓ $(\cdot 10^{-2})$	PR-AUC ↑	FPAR ↓	MSE ↓ $(\cdot 10^{-2})$	PR-AUC ↑	FPAR ↓	MSE ↓ $(\cdot 10^{-2})$	PR-AUC ↑	FPAR ↓
$\text{DIFF}_{\text{Dif.}}$	5.87 ± 0.24	0.14 ± 0.01	0.91 ± 0.01	3.21 ± 0.09	0.03 ± 0.00	0.97 ± 0.00	4.28 ± 0.09	0.14 ± 0.01	0.90 ± 0.00
DIFF_{VAE}	5.88 ± 0.32	**0.33 ± 0.02**	0.87 ± 0.01	2.58 ± 0.08	0.03 ± 0.00	0.97 ± 0.00	4.22 ± 0.09	0.16 ± 0.01	0.89 ± 0.00
$\text{CF}_{\text{Dif.}}$	4.37 ± 0.29	0.23 ± 0.01	0.77 ± 0.02	1.33 ± 0.07	**0.14 ± 0.01**	**0.87 ± 0.01**	2.49 ± 0.12	0.43 ± 0.01	0.62 ± 0.01
$\text{EG (CF)}_{\text{Dif.}}$	4.26 ± 0.28	0.26 ± 0.01	0.77 ± 0.01	1.32 ± 0.07	**0.14 ± 0.01**	**0.87 ± 0.01**	2.48 ± 0.12	0.44 ± 0.01	0.62 ± 0.01
CF_{VAE}	**4.16 ± 0.31***	0.32 ± 0.02	**0.72 ± 0.02***	1.34 ± 0.07	0.13 ± 0.01	0.88 ± 0.01	2.45 ± 0.12	0.45 ± 0.01	**0.61 ± 0.01***
$\text{EG (CF)}_{\text{VAE}}$	4.17 ± 0.30	0.31 ± 0.02	0.74 ± 0.02	**1.31 ± 0.07***	**0.14 ± 0.01**	**0.87 ± 0.01***	**2.42 ± 0.12***	**0.46 ± 0.01***	0.62 ± 0.01

As discussed in the main text, counterfactual explanation is a related concept in explainability, where the counterfactual (or more specifically, the difference between the input and the counterfactual denoted as $(x - \hat{\text{CF}})$) directly serves as the explanation instead of using it as a baseline for another method like IG. One limitation is that a raw pixel-wise difference between the input and its counterfactual highlights regions of change, but it does not necessarily convey which of these changes are influential for the model's prediction. This distinction is critical because not all observed differences are semantically meaningful or clinically relevant. For example, minor intensity variations or artifacts introduced during counterfactual generation may appear prominently in the difference map, even though they have negligible impact on the decision-making process. This can become problematic, as quality degrades rapidly when the counterfactual is imperfect. Generated counterfactuals are rarely perfect, and the raw difference then captures spurious variation across the entire image rather than localizing to the pathologically relevant region. Consequently, relying solely on raw differences risks misinterpretation by suggesting importance where none exists.

In contrast, path-based attribution methods such as IG and its extension EG provide a principled approach to quantifying feature importance. These methods compute attributions along a continuous interpolation path between a baseline and the input, effectively capturing how the model's output changes as features transition from the baseline state to the observed state. This mechanism allows IG/EG to distinguish meaningful changes that influence the prediction from incidental variations. Furthermore, these methods satisfy key axiomatic properties, including sensitivity and implementation invariance [44], which ensure theoretical soundness and consistency. A simple difference map does not guarantee these properties and therefore lacks the robustness required for reliable interpretability.

This advantage of IG based approaches becomes clear in the results, where the difference to the baseline (denoted $\text{DIFF}_{\text{Dif.}}$ and DIFF_{VAE}) is resulting in significantly worse scores in almost any metric and data set. The ablation test results of $\text{DIFF}_{\text{Dif.}}$ and DIFF_{VAE} can be seen in Fig. 9 (mass-center ablation) and Fig. 10 (top-k ablation). The overlap results can be seen in Table 4. As can be seen, our baseline choices are significantly outperforming $\text{DIFF}_{\text{Dif.}}$ and DIFF_{VAE} in almost any metric.

For a qualitative comparison, Fig. 11 includes examples of using the difference map as attribution. When compared to the attributions generated by our proposed approaches, it can be observed that many regions (not only the region of interest) are highlighted, making it hard to identify where the model actually focuses on for its decision.

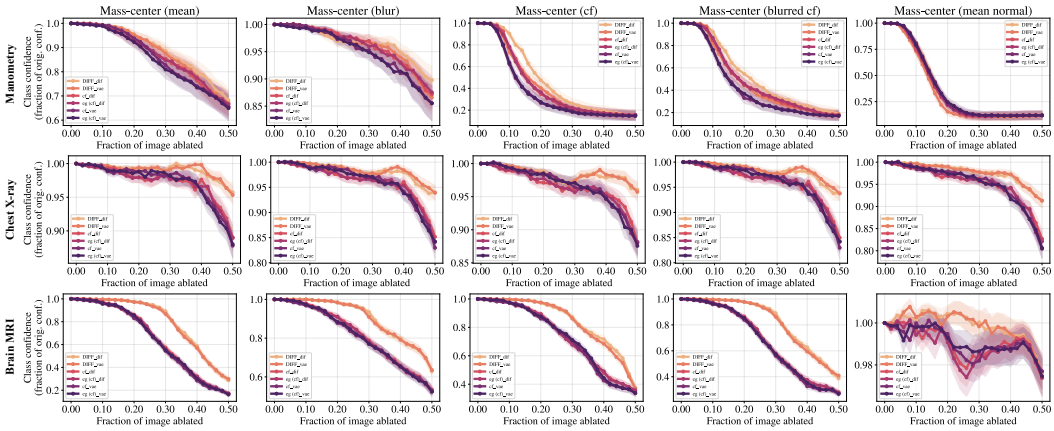


Figure 9: Results of the mass-center ablation tests, comparing our concepts to using the difference between counterfactual and input as attribution.

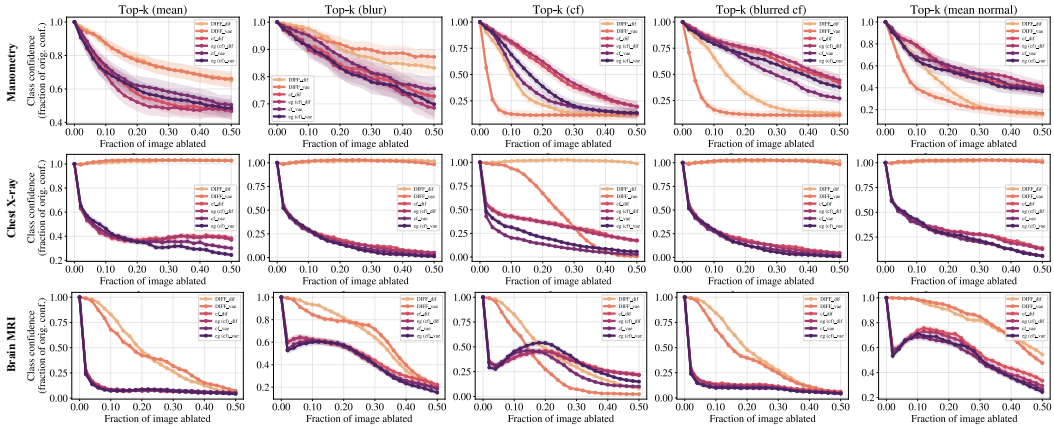
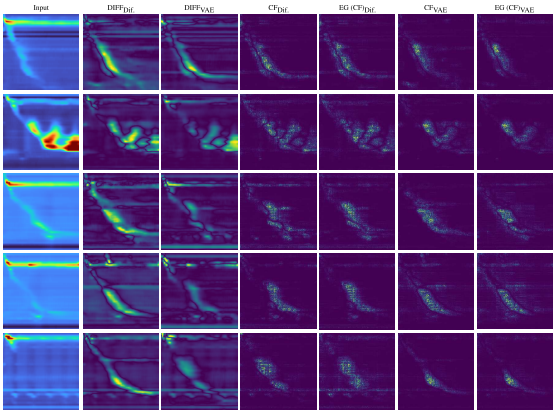
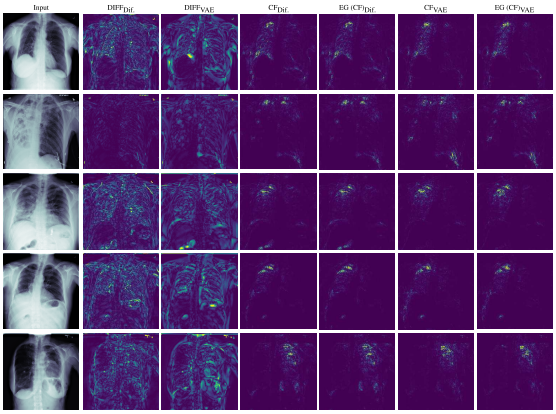


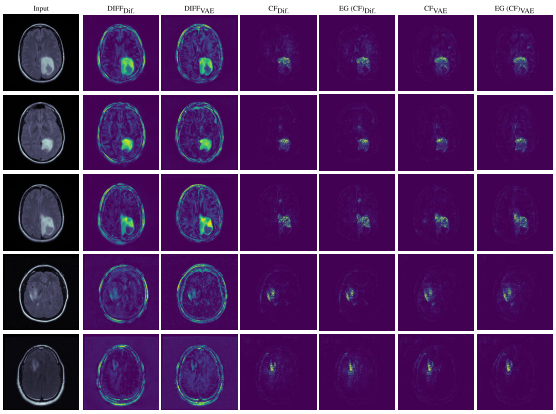
Figure 10: Results of the Top-k ablation tests, comparing our concepts to using the difference between counterfactual and input as attribution.



(a) Manometry



(b) Chest X-ray



(c) Brain MRI

Figure 11: Five examples from each data set for a qualitative comparison of direct counterfactual explanations (i.e. difference between counterfactual and input) and the attributions obtained by counterfactual baselines.

E Comparison to other baseline choices, related works, and why a counterfactual is needed

Table 5: Aggregated scores (mean ± se) comparing proposed baselines to alternative baseline choices; $p < 0.01$ (*)

	Manometry			Chest X-ray			Brain MRI		
Baseline	MSE ↓ $(\cdot 10^{-2})$	PR-AUC ↑	FPAR ↓	MSE ↓ $(\cdot 10^{-2})$	PR-AUC ↑	FPAR ↓	MSE ↓ $(\cdot 10^{-2})$	PR-AUC ↑	FPAR ↓
Mean (n)	4.46 ± 0.26	0.21 ± 0.02	0.81 ± 0.01	1.44 ± 0.07	0.11 ± 0.01	0.91 ± 0.01	2.95 ± 0.12	0.18 ± 0.01	0.83 ± 0.01
Rand (n)	4.57 ± 0.28	0.18 ± 0.02	0.83 ± 0.01	1.60 ± 0.07	0.07 ± 0.01	0.94 ± 0.00	2.70 ± 0.12	0.28 ± 0.01	0.75 ± 0.01
EG (n)	4.40 ± 0.25	0.24 ± 0.02	0.82 ± 0.01	1.48 ± 0.07	0.12 ± 0.01	0.92 ± 0.00	2.54 ± 0.11	0.37 ± 0.01	0.74 ± 0.01
LIG [14]	4.37 ± 0.29	0.24 ± 0.02	0.80 ± 0.02	1.52 ± 0.07	0.04 ± 0.00	0.96 ± 0.00	3.09 ± 0.12	0.15 ± 0.01	0.84 ± 0.01
CF-IG [15]	4.43 ± 0.28	0.20 ± 0.01	0.81 ± 0.01	1.43 ± 0.07	0.12 ± 0.01	0.90 ± 0.01	2.72 ± 0.13	0.31 ± 0.01	0.72 ± 0.01
GIG [25]	4.50 ± 0.29	0.19 ± 0.02	0.85 ± 0.01	1.52 ± 0.06	0.12 ± 0.01	0.92 ± 0.01	2.51 ± 0.12	0.39 ± 0.01	0.65 ± 0.01
IG2 [51]	4.76 ± 0.30	0.11 ± 0.01	0.88 ± 0.01	1.55 ± 0.08	0.04 ± 0.00	0.96 ± 0.00	3.17 ± 0.13	0.07 ± 0.00	0.91 ± 0.00
$CF_{Dif.}$	4.37 ± 0.29	0.23 ± 0.01	0.77 ± 0.02	1.33 ± 0.07	**0.14 ± 0.01**	**0.87 ± 0.01**	2.49 ± 0.12	0.43 ± 0.01	0.62 ± 0.01
EG $(CF)_{Dif.}$	4.26 ± 0.28	0.26 ± 0.01	0.77 ± 0.01	1.32 ± 0.07	**0.14 ± 0.01**	**0.87 ± 0.01**	2.48 ± 0.12	0.44 ± 0.01	0.62 ± 0.01
CF_{VAE}	**4.16 ± 0.31**	**0.32 ± 0.02**	**0.72 ± 0.02***	1.34 ± 0.07	0.13 ± 0.01	0.88 ± 0.01	2.45 ± 0.12	0.45 ± 0.01	**0.61 ± 0.01***
EG $(CF)_{VAE}$	4.17 ± 0.30	0.31 ± 0.02	0.74 ± 0.02	**1.31 ± 0.07***	**0.14 ± 0.01**	**0.87 ± 0.01***	**2.42 ± 0.12***	**0.46 ± 0.01***	0.62 ± 0.01

Related approaches As discussed in the main text, since our approach is conceptually distinct, yet grounded in similar underlying principles, we compare it to LIG [14] (see our implementation details below) and CF-IG [15], as well as to the adaptive path methods GIG [25], and IG2 [51]. Table 5 presents the results. As can be seen across all evaluated datasets, our baselines consistently outperform the other approaches in terms of attribution quality. For a qualitative comparison, Fig. 14 includes examples of using the related concepts. When compared to the attributions generated by our proposed approaches, more spurious and less precise attributions can be observed.

Other alternative baselines Additionally, as highlighted in the main text, one might consider using samples from the normal class as a more natural and computationally efficient baseline for attribution methods such as IG. This approach would avoid the need to generate a dedicated counterfactual for each input and instead rely on representative samples from the distribution of healthy or non-anomalous data. To evaluate the effectiveness of this strategy, we conduct additional experiments using three alternative baseline choices:

- Mean (n): the mean of all normal samples
- Rand (n): a single random normal sample
- EG (n): EG with 50 random normal samples

The results of these experiments, presented in Table 5, reveal that these baselines are consistently outperformed by the counterfactual-based approaches CF and EG (CF). This performance gap highlights the limitations of using generic normal samples, which may not be sufficiently tailored to the specific input being explained. In particular, normal samples may differ significantly in structure, intensity, or semantic content from the input, leading to attribution maps that are less focused and less informative. Additionally, we also perform ablation tests, comparing our approaches to the additional baselines Mean (n), Rand (n), and EG (n), as well as to the related approaches. The results can be seen in Fig. 12, confirming the consistently better performance of our proposed concept compared to all other approaches. For a qualitative comparison, Fig. 14 includes examples of using the alternative approaches. When compared to the attributions generated by our proposed approaches, more spurious and less precise attributions can be observed. These results further strengthen our argument that a baseline tailored to the input is achieving more accurate attribution results.

Implementation of Latent Integrated Gradients (LIG) We provide a short explanation of LIG as well as our implementation details of it. The original definition of LIG by Dravid et al. [14] is formulated as:

$$\text{LIG} = [\mathcal{G}(z_1, z_2) - \mathcal{G}(z_1, \mathbf{0})] \cdot \int_{\alpha=0}^{1} \frac{\partial \mathcal{C}\left(\mathcal{G}(z_1, \mathbf{0} + \alpha z_2)\right)}{\partial x} \, d\alpha \tag{22}$$

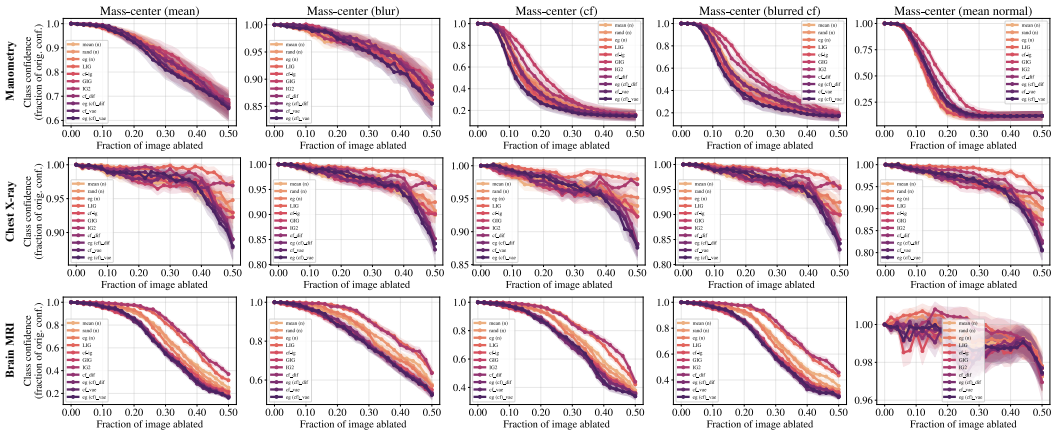


Figure 12: Results of the mass-center ablation tests when comparing the additional baseline and explainability concepts

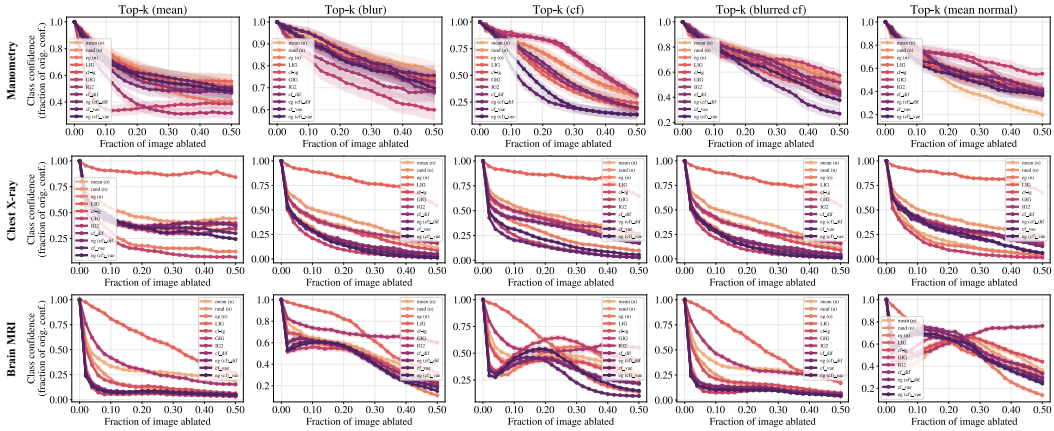


Figure 13: Results of the Top-k ablation tests when comparing the additional baseline and explainability concepts

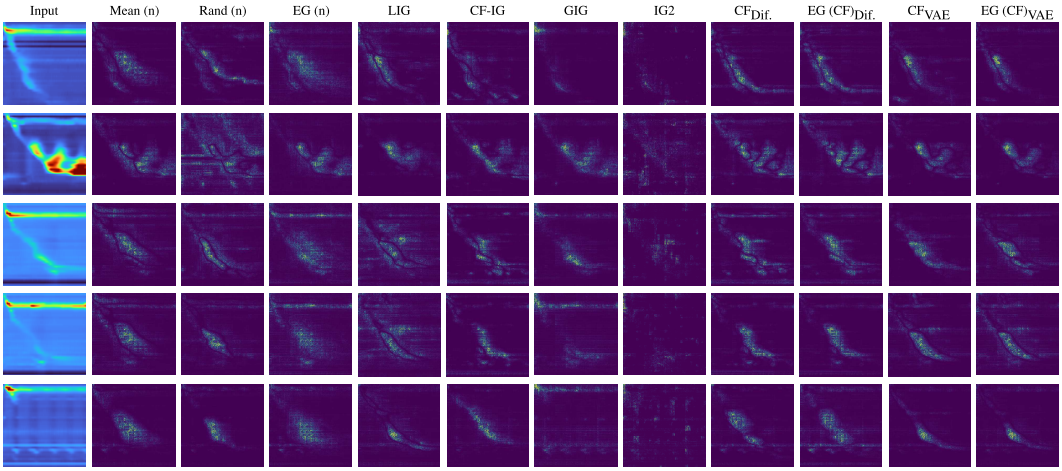
$\mathcal{G}$ is the generator of a GAN that takes two input latent vectors z_1, z_2, with z_1 corresponding to anatomical structure and z_2 corresponding to pathology features. Consequently, $\mathcal{G}(z_1, z_2)$ represents a "positive" (pathological) realization, while $\mathcal{G}(z_1, \mathbf{0})$ represents a "negative" (counterfactual healthy) realization. The LIG is then obtained by integrating gradients along an interpolation path in the latent space between these two realizations. A key limitation of this formulation is that the interpolation path consists entirely of synthetic samples, none of which correspond to the original input image. As a result, the quality and reliability of the attributions depend heavily on the generator's ability to produce realistic and semantically consistent outputs. This assumption is particularly daring in the medical imaging domain, where even subtle deviations from real data can distort pathological cues and lead to misleading interpretations.

For our comparison, we adjusted the formulation of LIG to work with our VAE setup instead of the original GAN setup. Specifically, we compute LIG with:

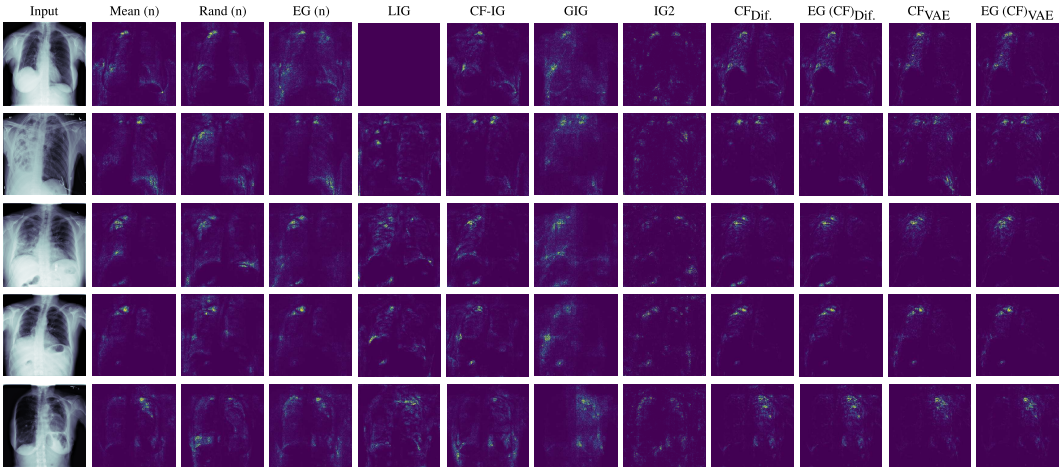
$$\text{LIG} = [\mathcal{D}(z_0) - \mathcal{D}(z^*)] \cdot \int_{\alpha=0}^{1} \frac{\partial \mathcal{C}\left(\mathcal{D}(z^*) + \alpha \cdot (\mathcal{D}(z_0) - \mathcal{D}(z^*))\right)}{\partial x} \, d\alpha \tag{23}$$

where z_0 is the latent encoding of input x, i.e. $z_0 = \mathcal{E}(x)$, and z^* is the latent representation of the counterfactual.

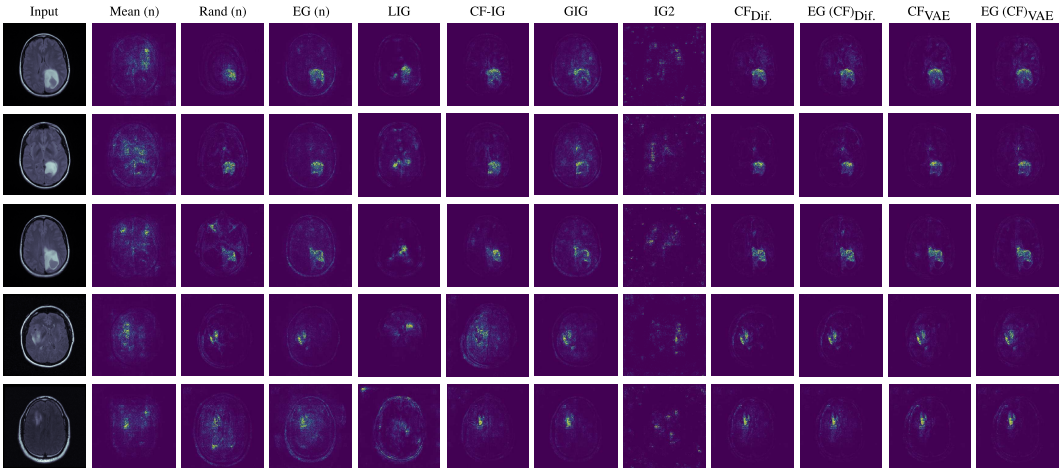
We acknowledge that LIG's performance is highly dependent on the quality of generated realizations, where a stronger generative model could improve attribution quality. However, this reliance underscores a fundamental limitation of LIG: the original input is excluded from the attribution process, making the explanation entirely dependent on the synthetic samples.



(a) Manometry



(b) Chest X-ray



(c) Brain MRI

Figure 14: Five examples from each data set for a qualitative comparison of the attributions obtained by different additional baseline choices and approaches.

F Limitations

While our approach improves attribution faithfulness in most evaluated scenarios, it introduces certain limitations. Computing baselines is more complex than using predefined ones, as our method requires training and sampling from a generative model, increasing computational overhead. We argue this trade-off is justified in medical contexts. While training the VAE and diffusion model incurs an upfront cost (dependent on hardware and training details), this is amortized over inference, where generating a counterfactual for a given input is lightweight. To demonstrate the computational efficiency, we measure training times of the VAE and diffusion model and inference times for computing counterfactual baselines. The results are reported in appendix J.

Additionally, the quality of generated baselines depends on the performance of the generative model. When the model fails to produce realistic or semantically meaningful counterfactuals, as observed especially in the Chest X-ray dataset, the baselines may not accurately represent the absence of class-defining features, limiting attribution reliability. In this aspect, we acknowledge that counterfactuals are artificial constructs and do not claim them as ground truth, but rather as more informative and plausible references than conventional baselines. Lastly, the interpretability of any explanation is constrained by the quality of the underlying classifier. While our classifiers performed reasonably well (see appendix K.3), even well-calibrated attributions are only as reliable as the model they explain.

G Quantitative assessment of realism of generated counterfactuals

Our theoretical framework (Proposition 2) establishes that attribution quality scales smoothly with the proximity of the generated counterfactual to the true counterfactual. While obtaining a perfect counterfactual is generally infeasible on real medical data, we provide empirical evidence that our generators produce counterfactuals which are both *distributionally aligned* with the real healthy manifold and *spatially targeted* at the diagnostically relevant regions, supporting the operational realization of semantic missingness.

Distributional realism via classifier-feature FID. We measure the distance between the distribution of generated counterfactuals and the distribution of real healthy images, using a modified Fréchet Inception Distance (FID) by employing the penultimate-layer features of the trained classifier (instead of a separate Inception model) as the embedding space. Working in the classifier's feature space ensures that distances reflect variation along axes the model itself uses to discriminate healthy from pathological inputs, which is the relevant notion of similarity for our setting.

To anchor the resulting numbers, we compute three reference distances: (i) FID between two disjoint splits of the real healthy set, which estimates the within-distribution noise floor; (ii) FID between real healthy and real pathological images, which provides an upper anchor reflecting the natural separation between the two classes; and (iii) FID between generated counterfactuals and the real healthy set, which measures how far our generated samples sit from the healthy distribution. Results for the brain MRI dataset are reported in Table 6.

Table 6: Classifier-feature FID between distributions across the three medical datasets. Lower values indicate greater distributional similarity. Both generators reduce the distance to the healthy distribution relative to the pathological inputs.

Comparison	**Manometry**	**Chest X-ray**	**Brain MRI**
Real healthy vs. real healthy (noise floor)	51.5	20.7	15.8
Real healthy vs. real pathological (upper anchor)	1038.2	414.1	1239.8
Real healthy vs. diffusion counterfactuals	485.8	266.5	416.1
Real healthy vs. VAE counterfactuals	443.2	388.1	291.1

Both generators reduce the distributional distance to the real healthy set relative to the pathological inputs on all data sets, indicating that the generated counterfactuals meaningfully shift the input toward the healthy manifold rather than producing arbitrary or off-manifold artifacts. The residual gap to the noise floor reflects a combination of finite-sample bias inherent to FID estimation, anatomy anchoring (counterfactuals are conditioned on pathological inputs and therefore retain patient-specific anatomical structure), and the natural imperfection of the generative models. Importantly, our framework does not require this gap to vanish: Proposition 2 guarantees that attribution quality improves continuously as the counterfactual approaches the true reference, and the framework is generator-agnostic, so improvements in counterfactual generation translate directly into improvements in attribution quality.

Spatial localization of counterfactual changes. A second, complementary criterion for a meaningful counterfactual is that the modifications introduced by the generator are concentrated in the diagnostically relevant region rather than distributed globally across the image. To assess this, we compute the average per-pixel change between the input x and the generated counterfactual x_{normal}, separately inside and outside the ground-truth pathology mask, and report the ratio:

$$r = \frac{\frac{1}{|M|}\sum_{i \in M} |x_i - x_{\text{normal},i}|}{\frac{1}{|\bar{M}|}\sum_{i \in \bar{M}} |x_i - x_{\text{normal},i}|},$$

where M denotes the pathology mask and $\bar{M}$ its complement. A ratio $r > 1$ indicates that changes are concentrated inside the clinically relevant region. Across all three datasets and both generators, we observe consistently $r > 1$ (Table 7), confirming that the generators selectively modify the pathological region while leaving surrounding anatomy largely intact.

Summary. Together, the FID-based distributional analysis and the localization analysis show that the generated counterfactuals (i) lie substantially closer to the real healthy distribution than the

Table 7: Ratio of average per-pixel change inside vs. outside the ground-truth pathology mask (mean $\pm$ se). Values > 1 indicate that the generators concentrate modifications in clinically relevant regions.

Comparison	**Manometry**	**Chest X-ray**	**Brain MRI**
Diffusion counterfactuals	2.04 ± 0.12	1.67 ± 0.04	3.24 ± 0.11
VAE counterfactuals	3.21 ± 0.18	1.70 ± 0.03	3.55 ± 0.10

pathological inputs and (ii) differ from the input primarily in the diagnostically relevant region. This provides empirical support that the generators produce counterfactuals which are operationally consistent with the notion of semantic missingness introduced in our work, while remaining within the approximation regime under which our theoretical guarantees hold.

H Dynamic counterfactual baseline generation

H.1 Dynamic counterfactual baseline generation using VAEs

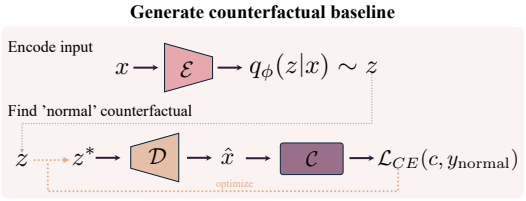


Figure 15: Overview of our approach to generate a counterfactual baseline z^* for input sample x.

This section contains more details on the optimization in the latent space of the VAE to generate the counterfactual baseline, as well as examples of the optimization path from pathological to counterfactual sample.

For a given input image $x \in \mathbb{R}^n$, we aim to find a "normal" counterfactual $\hat{x}^*$. To this end, we use a simple Convolutional Neural Network (CNN)-based VAE [28]. The VAE consists of an encoder $\mathcal{E} : \mathbb{R}^n \to \mathbb{R}^d$ and decoder $\mathcal{D} : \mathbb{R}^d \to \mathbb{R}^n$ and is trained to reconstruct input samples, i.e. $\mathcal{D}(\mathcal{E}(x)) = \hat{x} \approx x$. To obtain a latent representation $z \in \mathbb{R}^d$ of an input x, we can sample $z \sim q_\phi(z \mid x) := \mathcal{N}(\mu_\phi(x), \sigma^2_\phi(x)I)$, with$(\mu_\phi(x), \sigma^2_\phi(x)) = \mathcal{E}(x)$. The architecture details of the VAE can be found in appendix K.2.

The classifier $\mathcal{C} : \mathbb{R}^n \to \mathbb{R}^c$ maps the input to the predicted output logits for each possible output class, with one of the classes denoting the "healthy" (i.e. normal) class. In our experiments, we use a SwinTransformer-based [30] model for the classifier. The detailed architecture of the classifier can be found in appendix K.3.

To obtain a suitable counterfactual baseline $\hat{x}^*$ for input x, we aim to find the latent code $z^*(x)$ that, when decoded, minimizes the cross entropy loss to the normal class target y_n but is still sufficiently close to the input x otherwise, which can be formulated as:

$$z^*(x) \;=\; \arg\min_{z \in \mathbb{R}^d} \Big[\mathcal{L}_{CE}(\mathcal{C}(\mathcal{D}(z)), y_n) + \quad \lambda_{\text{sim}} \left\| x - \mathcal{D}(z) \right\|_2^2 \Big] \tag{24}$$

We perform this optimization by first obtaining an initial latent representation z_0 of the input x by $z_0 = \mathcal{E}(x)$. Then, we use gradient descent on z to minimize the cross entropy loss function $\mathcal{L}_{CE}(\mathcal{C}(\mathcal{D}(z_i)), y_{\text{normal}})$ using the Adam optimizer. This optimization proceeds until a confidence threshold of the normal class is reached:

$$z_{t+1} = z_t - \eta_t \cdot \texttt{Adam}\Big[\nabla_z \mathcal{L}_{CE}\big(\mathcal{C}(\mathcal{D}(z)), y_n\big) \Big] \tag{25}$$

In our implementation, we omit an explicit similarity term as in equation 24 by setting $\lambda_{\text{sim}} = 0$, since we are starting at $z_0 = \mathcal{E}(x)$ (where $\mathcal{D}(z_0)$) is already very close to x). During optimization, we stop once the desired confidence threshold is reached. The decoded image $\hat{x}^* = \mathcal{D}(z^*)$ is then used as the counterfactual baseline. An overview of the whole process can also be seen in Figure 15.

H.1.1 Optimization details

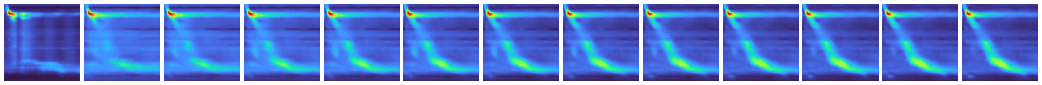
As described in section H.1, the counterfactual is found by traversing the latent space of the VAE (using the Adam optimizer) aiming to minimize the cross entropy loss between the decoded sample's predicted class and the true label. Table 8 shows the hyperparameters used to find the counterfactual. The parameters were chosen based on multiple runs and deemed suitable enough for our experiments.

Table 8: Optimization parameters

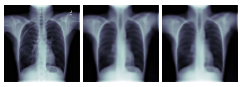
	Datasets		
Parameter	**Manometry**	**Chest X-ray**	**Brain MRI**
Learning rate	0.1	0.02	0.1
Max. iterations	50	50	50
Confidence threshold	0.99	0.99	0.99

H.1.2 Examples of path from pathological sample to normal counterfactual sample

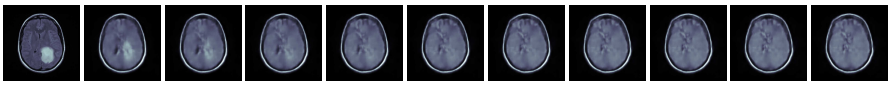
For illustration purposes, we show examples of decoded samples along the optimization path in Figure 16. The final counterfactual is reached once the specified confidence threshold is reached.



(a) Manometry



(b) Chest X-ray



(c) Brain MRI

Figure 16: Examples of decoded samples along the optimization path from the pathological sample to the counterfactual sample.

H.2 Dynamic counterfactual baseline generation using diffusion models

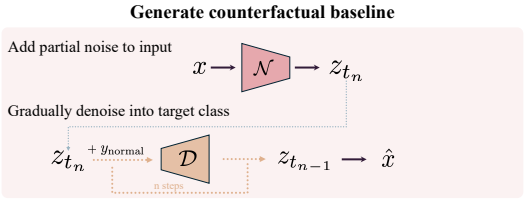


Figure 17: Overview of our approach to generate a counterfactual baseline z^* for input sample x.

For a given input image $x \in \mathbb{R}^n$, we aim to find a "normal" counterfactual $\hat{x}^*$ using a diffusion model operating directly in pixel space. The approach is based on a conditional denoising diffusion probabilistic model (DDPM) [21], in which a UNet-based denoising network $\epsilon_\theta : \mathbb{R}^n \times \mathbb{R} \times \mathcal{Y} \to \mathbb{R}^n$ is trained to predict the noise ϵ added to an input x at each diffusion timestep t, conditioned on a class label $y \in \mathcal{Y}$, by minimising:

$$\mathcal{L}_{\text{diff}} = \mathbb{E}_{x,\epsilon\sim\mathcal{N}(0,I),t}\left[\|\epsilon - \epsilon_\theta(x_t, t, y)\|_2^2\right] \tag{26}$$

where $x_t = \sqrt{\bar{\alpha}_t}\, x + \sqrt{1-\bar{\alpha}_t}\, \epsilon$ is the noised image at timestep t, and $\bar{\alpha}_t = \prod_{s=1}^{t}(1-\beta_s)$ is the cumulative product of a linear noise schedule $\{\beta_s\}_{s=1}^{T}$.

To enable classifier-free guidance (CFG) [20], the class conditioning is randomly dropped during training with probability p_{drop}, replacing y with a learned null token $\emptyset$, such that the model learns both conditional and unconditional noise prediction jointly. To obtain the counterfactual $\hat{x}^*$ for input x steered toward the normal class y_n, we follow a two-stage procedure. First, the input is partially noised to a timestep $t_{\text{start}} = \lfloor \rho \cdot T \rfloor$, controlled by a noise strength parameter $\rho \in (0, 1)$:

$$x_{t_{\text{start}}} = \sqrt{\bar{\alpha}_{t_{\text{start}}}}\, x + \sqrt{1-\bar{\alpha}_{t_{\text{start}}}}\, \epsilon, \quad \epsilon \sim \mathcal{N}(0, I) \tag{27}$$

This preserves the coarse structure of the input while introducing sufficient stochasticity for the model to transition toward the target class. The parameter ρ thus governs the tradeoff between structural similarity to the source and the freedom to deviate toward the target class.

Second, we perform a deterministic reverse diffusion from t_{start} to 0 using the DDIM sampler [41], with CFG applied at each step to steer the trajectory toward y_n:

$$\hat{\epsilon}_t = \epsilon_\theta(x_t, t, \emptyset) + s_{\text{cfg}} \cdot \left[\epsilon_\theta(x_t, t, y_n) - \epsilon_\theta(x_t, t, \emptyset)\right] \tag{28}$$

where $s_{\text{cfg}} \geq 1$ is the CFG scale, which controls how strongly the denoising trajectory is steered toward y_n. The predicted clean image at each step is then:

$$\hat{x}_0^{(t)} = \frac{x_t - \sqrt{1-\bar{\alpha}_t} \cdot \hat{\epsilon}_t}{\sqrt{\bar{\alpha}_t}} \tag{29}$$

and the DDIM update yields x_{t-1} from $\hat{x}_0^{(t)}$ and $\hat{\epsilon}_t$ without reintroducing stochasticity. The final counterfactual is the terminal denoised image $\hat{x}^* = \hat{x}_0^{(0)}$. The parameters ρ and s_{cfg} jointly govern how strongly the output is pushed toward the target class, and can be tuned depending on the degree of class transition required. An overview of the whole process can also be seen in Figure 17.

H.2.1 Optimization details

As described in section H.2, the counterfactual is found by adding noise to the input image and gradually denoise it towards the target class. Table 9 shows the hyperparameters used to create the counterfactual. The parameters were chosen based on multiple runs and deemed suitable enough for our experiments.

Table 9: Optimization parameters

	Datasets		
Parameter	**Manometry**	**Chest X-ray**	**Brain MRI**
Steps	50	50	50
s_{cfg}	15	7	7
ρ	0.7	0.2	0.7

I Details of data sets

Manometry High-resolution manometry (HRM) measures esophageal pressure during swallowing via a sensor-equipped catheter, producing pressure maps. It is the gold standard for diagnosing swallowing disorders. The data set, collected at TUM University hospital and annotated by medical specialists, includes six classes representing different contraction force categories.[1] Missingness is crucial in this data set, as several classes are defined by absent or reduced pressure.

Chest X-ray The data set[2] comprises chest X-rays for pneumothorax classification and segmentation tasks [50]. A pneumothorax, describing air in the pleural space, can appear as a dark region due to collapsed lung tissue, making missingness a relevant feature in this data set as well. The data set contains two classes, comprising normal and pathological samples.

Brain MRI The data set[3] comprises brain MRIs for tumor classification and segmentation tasks [8]. The data set contains two classes, comprising normal and pathological samples, with the tumors mostly visible as bright regions due to contrast agent.

The number of training, test and evaluation samples for each of the three data sets can be seen in Table 10. Train/test splits were either predefined (Chest X-ray, Brain MRI) or randomly selected (Manometry).

Table 10: Details of data sets

	Manometry	**Chest X-Ray**	**Brain MRI**
Training samples	3805	10675	3126
Test samples	922	1372	773
Distinct classes	6	2	2
Evaluation samples	80	263	277

[1] Ethical approval was obtained to use the collected data

[2] Available at: `https://www.kaggle.com/datasets/vbookshelf/pneumothorax-chest-xray-images-and-masks/data`

[3] Available at: `https://www.kaggle.com/datasets/mateuszbuda/lgg-mri-segmentation/data`

J Analysis of computational cost

While training the VAE and diffusion model introduces an upfront training time cost (where the exact cost is depending on the used hardware and training details), it is amortized over inference. The optimization of the latent code for a counterfactual is lightweight and performed for each input image during inference. We conducted measurements regarding the training times of the diffusion and VAE models and the inference time to compute the counterfactual baselines. The results, all of which were computed on a single NVIDIA L40S GPU, can be seen in Table 11 and Table 12. These results show that compute time during inference to generate a single counterfactual is very low (in the magnitude of at most $\sim$ 2.5 seconds). Furthermore, for the VAE approach we observe that the majority of compute time goes into optimizing within the latent space to find the counterfactual latent representation z^*. Sampling multiple perturbations around z^* for the EG (CF) case is then very efficient with almost no overhead. For the Diffusion model, the EG (CF) case takes more time, since every counterfactual is computed separately through the denoising process.

While this paper focuses purely on IG and extensions of it, we want to still give a brief section how the computational cost compares to other non-IG methods (e.g. SHAP). While it is true that SHAP and related methods do not require an explicit baseline in the same way as IG, they come with their own significant computational demands. For example, SHAP is based on computing Shapley values by evaluating all possible permutations of feature subsets. This leads to exponential complexity ($O(m \cdot 2^m)$) in the number of features m, making it intractable for high-dimensional inputs like images without approximations. Even approximations (such as KernelSHAP or DeepSHAP [31]) still require multiple forward passes per sample, often far exceeding the number of passes k needed for IG (which has complexity $O(k)$). This means that our method, while introducing a one-time cost for training the generative model, maintains a low and consistent computational demand during inference. Once the baseline is generated, IG is computed the same way as with any other traditional baseline using a fixed number of steps (as is common practice).

Table 11: Training time for the generative models (in minutes)

	Data sets		
	Manometry	**Chest X-ray**	**Brain MRI**
Diffusion	683.40	2436.73	747.63
VAE	33.24	65.34	28.21

Table 12: Computational time during inference to create counterfactual in seconds (mean $\pm$ std)

	Data sets		
Approach	**Manometry**	**Chest X-ray**	**Brain MRI**
$\mathsf{CF}_{\mathsf{Dif.}}$ (single counterfactual)	0.74 ± 0.09	0.09 ± 0.01	0.72 ± 0.00
$\mathsf{EG\ (CF)}_{\mathsf{Dif.}}$ (50 counterfactuals)	31.96 ± 2.24	3.76 ± 0.00	31.36 ± 0.03
$\mathsf{CF}_{\mathsf{VAE}}$ (single counterfactual)	2.44 ± 1.06	0.06 ± 0.04	2.15 ± 1.12
$\mathsf{EG\ (CF)}_{\mathsf{VAE}}$ (50 counterfactuals)	2.47 ± 1.06	0.07 ± 0.04	2.18 ± 1.12

K Model descriptions

In this section we provide the specifications of the models that are used in our work (i.e. the Diffusion model, VAE and classifier), as well as the training details.

K.1 Diffusion model

UNet architecture The UNet-based denoising network ϵ_θ follows a standard encoder-decoder structure with skip connections. The encoder progressively downsamples the input through a series of ResBlocks with strided convolutions, while the decoder upsamples back to the original resolution via transposed convolutions, with each decoder stage receiving the corresponding encoder feature map via channel-wise concatenation. A self-attention block is inserted at the bottleneck to capture global dependencies. At each stage, the timestep and class label are injected into the ResBlocks via adaptive group normalisation (AdaGN), which modulates the feature maps through a learned scale and shift derived from the combined timestep and label embedding. The architecture is summarised in Table 13.

Table 13: High-level UNet architecture of the diffusion denoising network ϵ_θ. Each ResBlock consists of two 3×3 convolutions with GroupNorm and SiLU activations, conditioned via AdaGN on the combined timestep and label embedding.

Stage	Type
Input conv	3×3 conv, $1 \to 128$ channels
Conditioning	
Timestep	Sinusoidal embedding, $2\times$ Linear + SiLU, $d_{\text{emb}} = 256$
Label	Learned embedding table(s), Linear + SiLU, $d_{\text{emb}} = 256$
Encoder (repeated 3 times, channels doubling each level)	
ResBlock	$128 \times 2^{l-1} \to 128 \times 2^{l}$ channels, AdaGN conditioned
Downsample	3×3 conv, stride 2
Bottleneck	
ResBlock + Attention + ResBlock	Self-attention between two AdaGN-conditioned ResBlocks
Decoder (repeated 3 times, channels halving each level)	
Upsample	2×2 transposed conv, stride 2
ResBlock	128×2^{l} + skip $\to 128 \times 2^{l-1}$ channels, AdaGN conditioned
Output	
GroupNorm + SiLU + 1×1 conv	$128 \to 1$ channel

Training details The diffusion models were trained using the AdamW optimizer and the hyper-parameters specified in Table 14. The hyperparameters were chosen based on a simple grid search. Figure 18 shows the loss on the training and validation sets during training of the diffusion model on the three data sets.

Table 14: Training parameters of the Diffusion model

	Datasets		
Parameter	**Manometry**	**Chest Xray**	**Brain MRI**
Input shape	128×128	128×128	128×128
Learning rate	0.0001	0.0001	0.0001
Batch size	64	64	64
Nr. of epochs	1000	1000	1000
Drop prob. (classifier-free guidance)	0.1	0.1	0.1
Timesteps	100	100	100

K.2 VAE

Encoder architecture The encoder architecture of the VAE used for the Manometry and Brain MRI data sets is depicted in Table 15, while the encoder architecture used for the Chest X-ray data set is depicted in Table 17. The main difference is the structure of the latent dimension, which is not

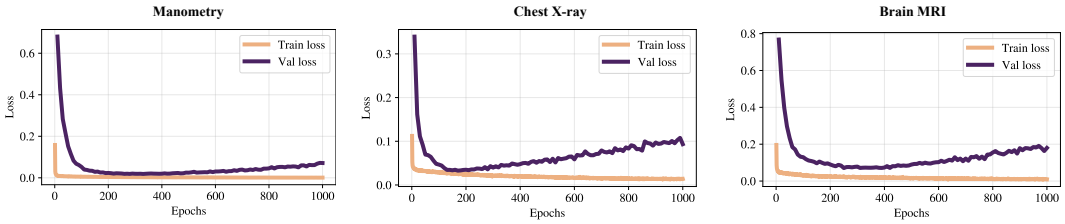


Figure 18: Loss on training and validation sets during training of the Diffusion model on the three data sets.

flattened but instead kept spatial for the latter. This architecture was chosen for the Chest X-ray data set due to better reconstruction results.

Decoder architecture The decoder architecture of the VAE used for the Manometry and Brain MRI data sets is depicted in Table 16, while the decoder architecture used for the Chest X-ray data set is depicted in Table 18.

Table 15: Encoder architecture of the convolutional VAE.

Layer	Type	Activation
Input	–	–
Conv1	4×4 conv, input $\rightarrow$ 32 channels, stride 2, padding 1	LeakyReLU
Conv2	4×4 conv, 32 $\rightarrow$ 64 channels, stride 2, padding 1	LeakyReLU
Conv3	4×4 conv, 64 $\rightarrow$ 128 channels, stride 2, padding 1	LeakyReLU
Conv4	4×4 conv, 128 $\rightarrow$ 256 channels, stride 2, padding 1	LeakyReLU
Conv5	4×4 conv, 256 $\rightarrow$ 512 channels, stride 2, padding 1	LeakyReLU
Flatten	–	–
FC_μ	Fully Connected	–
FC_σ	Fully Connected	–

Table 16: Decoder architecture of the convolutional VAE.

Layer	Type	Activation
Input	–	–
ConvTranspose1	4×4 conv, 512 $\rightarrow$ 256 channels, stride 2, padding 1	LeakyReLU
ConvTranspose2	4×4 conv, 256 $\rightarrow$ 128 channels, stride 2, padding 1	LeakyReLU
ConvTranspose3	4×4 conv, 128 $\rightarrow$ 64 channels, stride 2, padding 1	LeakyReLU
ConvTranspose4	4×4 conv, 64 $\rightarrow$ 32 channels, stride 2, padding 1	LeakyReLU
ConvTranspose5	4×4 conv, 32 $\rightarrow$ input channels, stride 2, padding 1	LeakyReLU
Sigmoid	–	–

Training details The VAEs were trained using the Adam optimizer and the hyperparameters specified in Table 19. The loss function is combination of the reconstruction loss and a $\beta-$weighted KL-Loss. The hyperparameters were chosen based on a simple grid search. Fig. 19 shows the loss on the training and validation sets during training of the VAE on the three data sets.

K.3 Classifier

Architecture Table 21 shows the abstracted architecture of the classifier that was used in our experiments. We use a swin_v2_t architecture with pretrained weights (ImageNet) as the classifier backbone. One classifier model was trained on one of the three data sets each.

Training details The model is trained using early stopping and we use the model from the epoch with the best accuracy on the validation set. The model is trained to output two separate classifications. The first is a binary classification, indicating if any disease is present or not, and the second one is a classification for the exact class of disease. (Since in the Chest X-ray data set and the Brain MRI

Table 17: Encoder architecture of the convolutional VAE with spatial latent space.

Layer	Type	Activation
Input	–	–
Conv1	4×4 conv, input $\rightarrow$ 32 channels, stride 2, padding 1	LeakyReLU
Conv2	4×4 conv, 32 $\rightarrow$ 64 channels, stride 2, padding 1	LeakyReLU
Conv3	4×4 conv, 64 $\rightarrow$ 128 channels, stride 2, padding 1	LeakyReLU
Conv4	4×4 conv, 128 $\rightarrow$ 256 channels, stride 2, padding 1	LeakyReLU
Conv5	4×4 conv, 256 $\rightarrow$ 512 channels, stride 2, padding 1	LeakyReLU
Conv μ	1×1 conv, 512 $\rightarrow Cz$ channels	–
Conv $\log \sigma^2$	1×1 conv, 512 $\rightarrow Cz$ channels	–

Table 18: Decoder architecture of the convolutional VAE with spatial latent space.

Layer	Type	Activation
Input	Spatial latent tensor $z \in \mathbb{R}^{C_z \times H_z \times W_z}$	–
Conv1	3×3 conv, $C_z \rightarrow 512$ channels, stride 1, padding 1	LeakyReLU
ConvTranspose1	4×4 conv, 512 $\rightarrow$ 256 channels, stride 2, padding 1	LeakyReLU
ConvTranspose2	4×4 conv, 256 $\rightarrow$ 128 channels, stride 2, padding 1	LeakyReLU
ConvTranspose3	4×4 conv, 128 $\rightarrow$ 64 channels, stride 2, padding 1	LeakyReLU
ConvTranspose4	4×4 conv, 64 $\rightarrow$ 32 channels, stride 2, padding 1	LeakyReLU
ConvTranspose5	4×4 conv, 32 $\rightarrow$ input channels, stride 2, padding 1	Sigmoid

data set only one disease is available, both heads are returning the same information). The classifiers are trained using a cross entropy loss function, weighted by the class counts to account for class imbalance. The optimizer used is Adam, with a cosine learning rate schedule. Fig. 20 shows the loss curves during training of the classifier, as well as the confusion matrix of the model from the epoch with the best results on the validation set. Additional hyperparameters are specified in Table 20. All hyperparameters were chosen based on few experimental runs.

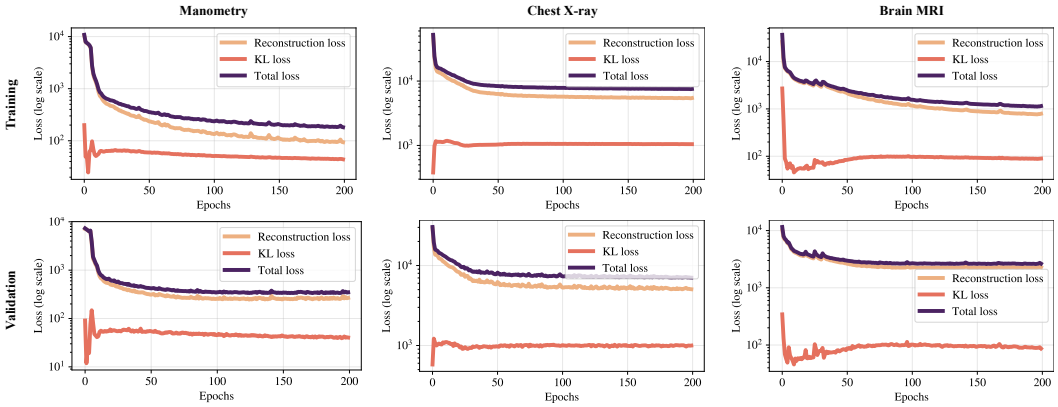


Figure 19: Loss on training and validation sets during training of the VAE model on the three data sets.

Table 19: Training parameters of VAE.

	Datasets		
Parameter	**Manometry**	**Chest Xray**	**Brain MRI**
Input shape	512×512	512×512	512×512
Learning rate	0.001	0.001	0.001
Batch size	256	256	256
Reconstruction loss	L2	L1	L2
β (weight of KL-Loss)	2	2	4
Nr. of epochs	200	200	200
Latent dimension	512	512	512

Table 20: Training parameters of classifier.

	Datasets		
Parameter	**Manometry**	**Chest Xray**	**Brain MRI**
Learning rate	3e-5	3e-5	3e-5
Weight decay	1e-4	1e-4	1e-4
Min. nr. of epochs	5	5	5
Max. nr. of epochs	50	50	50
Cosine scheduler warmup	4	4	4

Table 21: Abstracted architecture of the classifier.

Layer	**Type**	**Description**
Input	Preform Block	Conv2d layer that prepares input channels
Backbone	SwinTransformerV2	
Output	Classification Heads	Three attention pooling heads; one shallow and one deeper linear classification head with specified output dimensions;

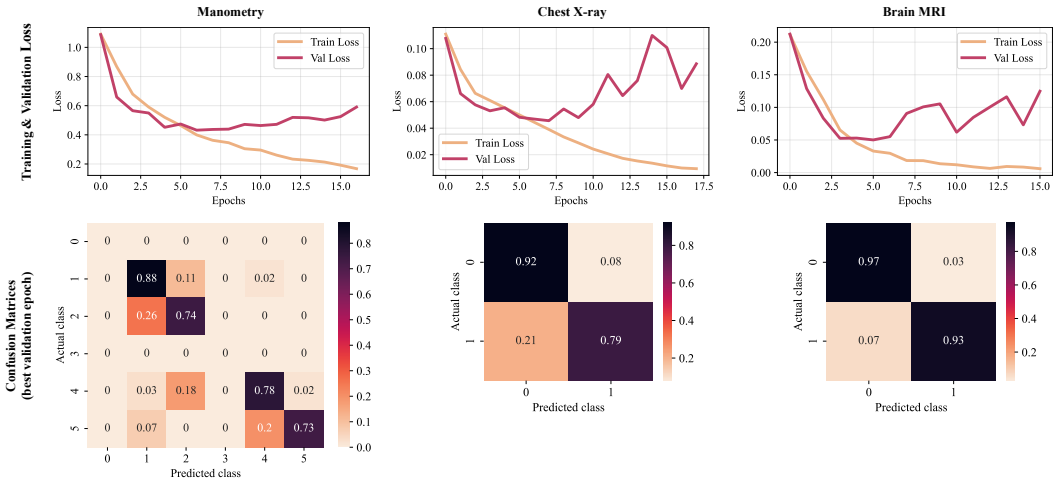


Figure 20: Loss on training and validation sets during training of the classifier (first row). Confusion matrices on the validation sets using of the model from the epoch with the best results on the validation set (second row).